UCLA
Computational and Applied Mathematics

Moving from Theory to Application: Evaluating the Numerical Implementation of Void Shape Effects and Damage Delocalization in the Modelling of Ductile Fracture in Porous Plastic Metals.

Koffi Enakoutsa
Yanni Bills

Department of Mathematics
University of California, Los Angeles
Los Angeles, CA, 90095-1555

Contents

List of Figures

List of Tables

1. Abstract

In this paper, we present a robust exploration of the Gologanu-Leblond-Devaux (GLD) model, an advanced iteration of Gurson's model, designed to predict ductile fractures in porous metals. Going beyond the limits of the original Gurson model, the GLD model accounts for cavity shape effects and nonlocal strain localization, marking a significant leap in fracture mechanics. We also present a comprehensive exposition of the GLD model and its nonlocal extension, establishing their compatibility with the concept of generalized standard materials. Notably, we emphasize the uniqueness of solutions in the numerical implementation, underlining the imperative need for a meticulously devised mixed implicit/explicit algorithm. Furthermore, we set out to validate the GLD model through rigorous comparisons of our numerical simulations with experimental data. Employing a damage delocalization approach rooted in the natural logarithm of porosity, our study provides compelling evidence of the model's performance. This approach mitigates issues observed with the original porosity rate, preventing excessive smoothing of porosity and maintaining the fidelity of stress-strain curves. Additionally, we gave a profound theoretical elucidation of this phenomenon via Fourier's analysis of porosity rate. Through this work, we not only enhance our understanding of ductile fracture behavior but also establish a robust numerical framework for its predictive modeling. The GLD model emerges as a powerful tool for the accurate analysis and prediction of fracture phenomena in porous materials, further advancing the field of materials science and engineering.

2. Introduction

The famous Gurson's model [5] , in the cases involving the behaviors of ductile porous metals, has already demonstrated its ability to predict several fracture problems involving ductile cracking. When incorporated in a finite element code, it has predicted the cup cone fracture phenomena of a round axisymmetric specimen ([8] and [13] .) It also has been applied to a wide range of materials and engineering problems over the years. Here are some examples of problems and materials where the Gurson model has been used to predict ductile fracture:

- Metallic Alloys: The Gurson model has been applied to various metallic materials, such as steel and aluminum alloys, to predict the initiation and propagation of ductile fractures in these materials under various loading conditions.
- Welded Joints: In welded structures, the presence of weld defects and inclusions can lead to ductile fracture. The Gurson model has been used to assess the integrity of welded joints and predict their fracture behavior.
- Sheet Metal Forming: During sheet metal forming processes, materials can undergo ductile fracture. The Gurson model has been employed to predict the onset and propagation of fractures in sheet metal components.
- Automotive Crashworthiness: When designing cars for crashworthiness, engineers need to understand how materials will deform and fracture during a collision. The Gurson model has been applied to analyze the ductile fracture behavior of automotive materials.
- Pipeline Integrity: In the oil and gas industry, pipelines are subject to high-pressure environments. The Gurson model has been applied to assess the ductile fracture resistance of pipeline materials, especially when dealing with defects or corrosion.
- Fracture in Polymers and Ceramics: While the original Gurson model was developed for metals, modified versions of the model have been extended to predict ductile fracture in polymers and ceramics.
- Composite Materials: The Gurson model has been adapted to predict the behavior of composite materials with voids, delaminations, or fiber-matrix debonding, aiding in the design of composite structures.
- Pipeline Integrity: In the oil and gas industry, pipelines are subject to high-pressure environments. The Gurson model has been applied to assess the ductile fracture resistance of pipeline materials, especially when dealing with defects or corrosion.

A drawback of this model is that it assumes that the existing cavities in the materials are spherical, neglecting hereby the effects of the cavities' shape on the

general mechanical behavior of the material. This is a good approximation when the triaxiality (ratio of the mean stress with respect to the equivalent von Mises stress) is very high; indeed, the mean stress is then higher than the mean deviatoric stress such that the cavity has the tendency to grow in the same way in all of the directions. However, when the triaxiality is small the effects of the cavities' shape become important and the Gurson model predicts worse outcomes. For example, in a uniaxial tensile test, the triaxiality is $1/3$, and Gurson's model predicts a continuous increase of the porosity leading to coalescence of cavities and eventual failure.

In reality, however, the cavities quickly become cylindrical under the effect of the tensile stress exerted, and the porosity then ceases to grow in the manner one might expect. This surprising phenomenon challenges the predictions of the Gurson model, which assumes that porosity growth is primarily governed by the average stress, typically positive in tensile loading scenarios. Instead, the dominant factor influencing cavity growth in this context is the lateral constraint, which interestingly approaches zero as the cavities transform into more cylindrical shapes.

Another intriguing scenario where the shape effects of cavities play a crucial role is when these voids take the form of cracks, often manifesting as very flattened voids. These cracks can be generated, for instance, through the rupture of a brittle phase within the material. In such cases, the geometrical characteristics of these cracks, their orientation, and their interaction with the surrounding material become critical factors that significantly influence the material's mechanical behavior and failure mechanisms, see for instance Li and Huang [21], Monchiet *et al.* [25] , Wen *et al.* [22] , Li and Steinmann [28]. Understanding and modeling these intricate shape effects of cavities and cracks is of paramount importance in advancing our comprehension of material behavior under various loading conditions and enhancing our ability to engineer materials with tailored properties.

Gologanu *et al.* [19] made a significant contribution to the field of material science and structural mechanics by extending Gurson's pioneering model to incorporate the influence of cavity shape characteristics. While Gurson's model laid the foundation for understanding the behavior of materials with voids or cavities, Gologanu *et al.* took this a step further. Their groundbreaking work recognized that real-world cavities often deviate from idealized spherical shapes and, as a result, introduced a novel parameter known as the shape factor. This shape factor is a crucial addition to the model, as it accounts for the non-spherical nature of cavities, enabling a more accurate representation of the complex void geometries found in materials.

The concept of the shape factor introduced by Gologanu *et al.* is particularly valuable in cases where voids exhibit axisymmetric ellipsoidal shapes. By considering the ratio of the axes of these ellipsoids, the shape factor allows engineers and researchers to better capture the intricate details of cavities within materials. This enhancement not only improves the accuracy of the model but also enhances our understanding of how cavity shape influences the overall mechanical behavior of

materials.

Also, constitutive models involving softening all predict unlimited localization of strain and damage. This feature generates such undesired phenomena as absence of energy dissipation during crack propagation and mesh size sensitivity in finite element computations. Gurson [5] 's famous model for porous ductile materials, which was derived from approximate limit-analysis of some elementary voided cell in a plastic solid, is no exception. In this model, unlimited localization arises from the softening because of the gradual increase of the porosity.

Several proposals have been made to solve this problem. One of these, attributed to Leblond *et al.* [16] but based on a previous suggestion made by Pijaudier-Cabot and Bazant *et al.* [9] in damage of concrete, comprises adopting a nonlocal evolution equation for the porosity involving some spatial convolution of some "local porosity rate" within an otherwise unmodified Gurson model. This simple proposal has attracted the attention of several authors (Tvergaard and Needleman [18], Tvergaard and Needleman [20], Enakoutsa *et al.* [23, 24]). It was notably checked by Tvergaard and Needleman [18] that it allows to eliminate mesh size effects. Also, Enakoutsa *et al.* [23, 24] showed that with a minor modification, it leads to an excellent numerical reproduction of the results of typical experiments of ductile rupture.

One shortcoming of Leblond *et al.* [16]'s proposal, however, is that it is purely heuristic and lacks any serious theoretical justification. This was the motivation for a later, more elaborate and physically based proposal of Gologanu *et al.* [19]. These authors derived an improved variant of Gurson's model (the *GLPD model*[1]) through some refinement of this author's original homogenization procedure based on Mandel [1]'s and Hill [2]'s classical conditions of homogeneous boundary strain rate. In the approach of Gologanu *et al.* [19], the boundary velocity is assumed to be a quadratic, rather than linear, function of the coordinates. The physical idea is to account in this way for the possibility of quick variations of the macroscopic strain rate, such as encountered during strain localization, over short distances of the order of the size of the elementary cell considered. The output of the homogenization procedure is a model of "micromorphic" nature involving the second gradient of the macroscopic velocity and generalized macroscopic stresses of "moment" type (homogeneous to the product of a stress and a distance), together with some "microstructural distance" connected to the mean spacing between neighboring voids. Practical applications from a theoretical and experimental stand-point have found this model very useful, see for instance Enakoutsa [27, 29]

The objective of this paper is to present the numerical implementations of this GLD model and its nonlocal extension into a finite element code and assessment the robustness of this numerical implementation by comparing the numerical pre-

[1] GLPD: Gologanu-Leblond-Perrin-Devaux.

dictions of the model with available experimental data for typical ductile fracture test specimens. The rest of the paper is organized as follows.

- In Section 3, we initially provide a concise overview of GLD original model, as well as the nonlocal extension introduced by Leblond *et al.* [16].
- Following this, in anticipation of delving into its numerical application, Section 3 examines its connection to the category of generalized standard materials, a concept delineated and explored by Halphen and Nguyen [3]. It is demonstrated that both the initial model and its altered iterations define such a material, assuming that porosity remains constant, the orientation, and the shape of the cavity are kept constant.
- Section 4 proceeds to address the numerical implementation of the GLD model. As per the property established in Section 3, it is affirmed that the problem of projecting the elastically computed stress tensor onto the yield locus (plastic correction of the elastic predictor) has a unique solution. This is valid when the equations concerning this problem are derived using implicit time discretization for the plastic strain and hardening parameter components, but explicit time discretization is employed for the porosity, the orientation, and the shape factor components. This serves as a compelling rationale for embracing a "mixed" implicit/explicit algorithm
- Following this, in Section 5, we conduct a comparison between the results obtained from numerical simulations illustrating the fracture behavior of a standard axisymmetric pre-cracked specimen and the experimental observations reported by Rousselier and Mudry [7]. All the simulations employ a damage delocalization approach based on the natural logarithm of porosity. This decision is motivated by the observation that using the original porosity rate leads to excessive smoothing of the porosity, resulting in a sharp decline in the stress-strain curves after the onset of coalescence, as noted in Enakoutsa [23] and Enakoutsa *et al.* [24]. In this same section, we provide a theoretical explanation of this excessive smoothing of the porosity based on some Fourier analysis of the porosity rate.

3. Theoretical equations of the model

3.1. Overview of the model

The constitutive equations of the model was derived by Gologanu *et al.* [14, 17]. The work of Gologanu *et al.* is characterized by their endeavor to incorporate void shape effects into "homogenized" models for porous plastic metals. They achieve this by extending Gurson's [5] classical limit-analysis of a hollow sphere to encompass an axisymmetric prolate or oblate spheroid containing a spheroidal confocal cavity, akin to their approach in previous works. While their primary focus lies on axisymmetric loadings, they also present some generalization of the model to arbitrary loadings towards the end of their study.

In their work, Gologanu *et al.* [14, 17] introduce the family of axisymmetric velocity fields initially proposed by Lee and Mear [12]. These fields are supplemented to account for the finite nature of the representative volume, in contrast to the infinite medium considered by Lee and Mear [12]. Gologanu *et al.* [14, 17] then describe the derivation of the exact macroscopic yield locus or an approximate one from these velocity fields. By utilizing only two trial velocity fields, as opposed to a larger number, they simplify the process of obtaining an analytic, approximate yield function. This approach enables them to calculate overall plastic dissipation based on the two independent components of the macroscopic strain rate, leading to the derivation of an approximate criterion that reproduces well-known exact or widely accepted results.

3.2. Constitutive equations of the model

The voids are assumed ellipsoidal axisymmetric and aligned, of axis $\mathbf{e}_3$ [2]. The porosity f is defined as the ratio of the voids to the total volume of matter and voids. The shape factor of the cavity is defined as the logarithm of the ratio of the axes of a cavity according to $\mathbf{e}_3$ and a perpendicular direction.

3.2.1. Plasticity criterion, evolution equations of the internal parameters

The yield criterion, which depends on the porosity f, the parameter of the shape factor S and a strain hardening parameter $\overline{\sigma}$ representing some "average of the elastic limit of the sound matrix," is written as

$$\begin{aligned}\Phi(\boldsymbol{\sigma}, f, S, \overline{\sigma}) \equiv & \frac{C}{\overline{\sigma}^2}\|\boldsymbol{\sigma}' + \eta\sigma_h \boldsymbol{X}\|^2 + 2q(g+1)(g+f)cosh(K\frac{\sigma_h}{\overline{\sigma}}) \\ & - (g+1)^2 - q^2(g+f)^2 = 0.\end{aligned} \tag{1}$$

In this expression, $\boldsymbol{\sigma}'$ represents the deviatoric stress $\boldsymbol{\sigma}$, $\mathbf{X}$ the tensor defined as

$$\boldsymbol{X} = \frac{1}{3}(-\boldsymbol{e}_1 \otimes \boldsymbol{e}_1 - \boldsymbol{e}_2 \otimes \boldsymbol{e}_2 + 2\boldsymbol{e}_3 \otimes \boldsymbol{e}_3) \tag{2}$$

[2] the voids' principal basis being $(\mathbf{e}_1, \mathbf{e}_2, \mathbf{e}_3)$

(where we recall that the vector $\mathbf{e}_3$ is parallel to the axes of the voids), and $||\,||$ the von Mises norm:

$$\|\boldsymbol{T}\| \equiv \left(\frac{3}{2}\boldsymbol{T} : \boldsymbol{T}\right)^{1/2} = \left(\frac{3}{2}\boldsymbol{T}_{ij}\boldsymbol{T}_{ij}\right)^{1/2}; \tag{3}$$

we shall adopt in the rest of this note the simplified notation

$$\sigma_{eq} \equiv \|\boldsymbol{\sigma}' + \eta\sigma_h \boldsymbol{X}\| \tag{4}$$

(note that with this definition , $\sigma_{eq} \neq ||\boldsymbol{\sigma}'||$ as it is customary).

The parameters C, η, K, g depend uniquely on f and S; their expressions are given in Gologanu *et al.* [19] but are not necessary here. In addition, the stress σ_h is

$$\sigma_h = \alpha_2(\sigma_{11} + \sigma_{22}) + (1 - 2\alpha_2)\sigma_{33} \tag{5}$$

where here also, α_2 is a parameter which depends uniquely on f and S whose expressions are given in Gologanu *et al.* [19] . Finally, q is the "Tvergaard's parameter [6] " whose value depends here of the shape of the cavities given in Gologanu *et al.* [19] .

The law of evolution of porosity is classically deduced from the approximated incompressibility (the elasticity being neglected) of the sound matrix:

$$\dot{f} = 3(1 - f)\dot{\boldsymbol{\varepsilon}}^p_m \tag{6}$$

where $\dot{\varepsilon}^p_m = \frac{1}{3}tr(\dot{\boldsymbol{\varepsilon}}^p)$ represents the mean part of the strain rate $\dot{\boldsymbol{\varepsilon}}^p$. The law of the evolution of the shape factor of cavities is as follows

$$\dot{S} = \frac{3}{2}h\dot{\varepsilon}^{p'}_{33} + 3\left(\frac{1 - 3\alpha_1}{f} + 3\alpha_2 - 1\right)\dot{\varepsilon}^p_m \tag{7}$$

where $\dot{\boldsymbol{\varepsilon}}^{p'}$ represents the deviatoric strain rate of the plastic deformation $\dot{\boldsymbol{\varepsilon}}^p$, $\dot{\varepsilon}^p = \frac{1}{3}tr\dot{\boldsymbol{\varepsilon}}^p$ its mean part as above and α_1 a parameter depending here also on the parameters f and S and whose precise expression is given in Gologanu *et al.* [19]. Finally, h is a parameter depending, in addition to f and S, on the triaxiality T defined by

$$T = \frac{\sigma_m}{\|\boldsymbol{\sigma}'\|} \tag{8}$$

where $\sigma_m = \frac{1}{3} tr\boldsymbol{\sigma}$ is the mean part of the stress tensor. The parameter $\overline{\sigma}$ is given as a function of a strain hardening parameter $\overline{\varepsilon}$ representing roughly the average equivalent deformation of the sound matrix by the formula

$$\overline{\sigma} = \sigma(\overline{\varepsilon}) \tag{9}$$

where $\sigma(\overline{\varepsilon}$ represents the function given the Cauchy stress as a function of the logarithmic deformation in a simple tensile test on the sound material. The evolution equation of $\overline{\varepsilon}$ is the same as the one proposed by Gurson

$$(1-f)\overline{\sigma}\ \dot{\overline{\varepsilon}} = \boldsymbol{\sigma} : \dot{\boldsymbol{\varepsilon}}^p. \tag{10}$$

Finally, the evolution equation of $\mathbf{x}_3$ parallel to the axis of the voids is given by

$$\dot{\boldsymbol{e}}_3 = \boldsymbol{\Omega} \cdot \boldsymbol{e}_3 \tag{11}$$

where $\boldsymbol{\Omega}$ is the "rotation rate of the matter" (for example the antisymmetric part of the velocity gradient.) This equation is based on the heuristic hypothesis that the voids and the matter has the same rotation rate.

3.2.2. Flow rule associated to the yield criterion by normality

As usual, we assume the partition of the total deformation rate $\dot{\boldsymbol{\varepsilon}}$ between the elastic deformation rate $\dot{\boldsymbol{\varepsilon}}^e$ and the plastic formation rate $\dot{\boldsymbol{\varepsilon}}^p$. The first rate is given by the usual elasticity law and the second by

$$\dot{\boldsymbol{\varepsilon}}^p = \dot{\lambda} \frac{\partial \Phi}{\partial \boldsymbol{\sigma}}, \quad \dot{\lambda} \geq 0 \tag{12}$$

where Φ represents (remember) the yield function and the plastic multiplier $\dot{\lambda}$. It is now a question of explaining this equation. To do this, let's start by evaluating

$$\begin{aligned}\frac{\partial \sigma_{eq}^2}{\partial \sigma_{ij}} =& \frac{\partial}{\partial \sigma_{ij}} \left[\frac{3}{2} \left(\sigma'_{kl} + \eta \sigma_h X_{kl} \right) \left(\sigma'_{kl} + \eta \sigma_h X_{kl} \right) \right] \\ &= 3 \left(\sigma'_{kl} + \eta \sigma_h X_{kl} \right) \left(\delta_{ik}\delta_{jl} - \frac{1}{3}\delta_{ij}\delta_{kl} + \eta \frac{\partial \sigma_h}{\partial \sigma_{ij}} X_{kl} \right) \\ &= 3 \left[\sigma'_{ij} + \eta \sigma_h X_{ij} + \left(\sigma'_{kl} + \eta \sigma_h X_{kl} \right) \eta \frac{\partial \sigma_h}{\partial \sigma_{ij}} X_{kl} \right] \\ &= 3 \left[\sigma'_{ij} + \eta \sigma_h X_{ij} + \frac{2}{3} \eta \frac{\partial \sigma_h}{\partial \sigma_{ij}} \left(\frac{3}{2} \boldsymbol{\sigma}' : \boldsymbol{X} + \eta \sigma_h \right) \right].\end{aligned}$$

As a result, the Greek indices taking only values 1 and 2 and taking into account the obvious relationships $\partial \sigma_h \Big/ \partial \sigma_{\alpha\beta} = \alpha_2 \delta_{\alpha\beta}$, $\partial \sigma_h \Big/ \partial \sigma_{\alpha 3} = 0$, $\partial \sigma_h \Big/ \partial \sigma_{33} = 1 - 2\alpha_2$, we get

$$\begin{aligned}\frac{\partial \Phi}{\partial \sigma_{\alpha\beta}} =& \frac{3C}{\overline{\sigma}^2} \left[\sigma'_{\alpha\beta} + \eta \sigma_h X_{\alpha\beta} + \frac{2}{3} \eta \alpha_2 \delta_{\alpha\beta} \left(\frac{3}{2} \boldsymbol{\sigma}' : \boldsymbol{X} + \eta \sigma_h \right) \right] \\ &+ 2q(g+1)(g+f) \frac{K}{\overline{\sigma}} \alpha_2 \delta_{\alpha\beta} sinh \left(K \frac{\sigma_h}{\overline{\sigma}} \right);\end{aligned}$$

$$\frac{\partial \Phi}{\partial \sigma_{\alpha 3}} = \frac{3C}{\overline{\sigma}^2} \sigma_{\alpha 3}; \tag{13}$$

$$\begin{aligned}\frac{\partial \Phi}{\partial \sigma_{33}} =& \frac{3C}{\overline{\sigma}^2} \left[\sigma'_{33} + \eta \sigma_h X_{33} + \frac{2}{3} \eta (1 - 2\alpha_2) \left(\frac{3}{2} \boldsymbol{\sigma}' : \boldsymbol{X} + \eta \sigma_h \right) \right] \\ &+ 2q(g+1)(g+f) \frac{K}{\overline{\sigma}} (1 - 2\alpha_2) sinh \left(K \frac{\sigma_h}{\overline{\sigma}} \right).\end{aligned}$$

As a consequence

$$\begin{aligned}\dot{\varepsilon}_m^p =& \frac{1}{3} \left(\dot{\varepsilon}_{\alpha\alpha}^p + \dot{\varepsilon}_{33}^p \right) = \frac{\dot{\lambda}}{3} \left(\frac{\partial \Phi}{\partial \sigma_{\alpha\alpha}} + \frac{\partial \Phi}{\partial \sigma_{33}} \right) \\ =& \frac{\dot{\lambda}}{3} \left[\frac{2C\eta}{\overline{\sigma}^2} \left(\frac{3}{2} \boldsymbol{\sigma}' : \boldsymbol{X} + \eta \sigma_h \right) + 2q(g+1)(g+f) \frac{K}{\overline{\sigma}} sinh \left(K \frac{\sigma_h}{\overline{\sigma}} \right) \right].\end{aligned} \tag{14}$$

In addition, combining Eqs. (12, 13, 14), we see that

$$\begin{aligned}
\dot{\varepsilon}^p_{\alpha\beta} =& \dot{\lambda} \cdot \frac{3C}{\overline{\sigma}^2} \left(\sigma'_{\alpha\beta} + \eta \sigma_h X_{\alpha\beta} \right) + \alpha_2 \delta_{\alpha\beta} \cdot 3\dot{\varepsilon}^p_m; \\
\dot{\varepsilon}^p_{\alpha 3} =& \dot{\lambda} \cdot \frac{3C}{\overline{\sigma}^2} \sigma_{\alpha 3}; \\
\dot{\varepsilon}^p_{33} =& \dot{\lambda} \cdot \frac{3C}{\overline{\sigma}^2} \left(\sigma'_{33} + \eta \sigma_h X_{33} \right) + (1 - 2\alpha_2) \cdot 3\dot{\varepsilon}^p_m.
\end{aligned} \tag{15}$$

Let us assume that

$$\dot{\boldsymbol{\varepsilon}}^p_d = \dot{\boldsymbol{\varepsilon}}^p - 3\alpha_2 \dot{\varepsilon}^p_m \boldsymbol{e}_\alpha \otimes \boldsymbol{e}_\alpha - 3(1 - 2\alpha_2) \dot{\varepsilon}^p_m \boldsymbol{e}_3 \otimes \boldsymbol{e}_3 \tag{16}$$

(It will be observed that $\dot{\boldsymbol{\varepsilon}}^p_d$ is a pure deviator, that is to say that $tr\dot{\boldsymbol{\varepsilon}}^p_d = 0$). From Eqs. (15, 16)

$$\dot{\boldsymbol{\varepsilon}}^p_d = \dot{\lambda} \frac{3C}{\overline{\sigma}^2} \left(\boldsymbol{\sigma}' + \eta \sigma_h \boldsymbol{X} \right).$$

Thus, the tensors $\dot{\boldsymbol{\varepsilon}}^p_d$ and $\boldsymbol{\sigma}' + \eta \sigma_h \boldsymbol{X}$ are positively collinear. We immediately deduce that

$$\dot{\boldsymbol{\varepsilon}}^p_d = \frac{3}{2} \frac{\dot{\varepsilon}^p_d}{\sigma_{eq}} \left(\boldsymbol{\sigma}' + \eta \sigma_h \boldsymbol{X} \right). \tag{17}$$

where

$$\dot{\varepsilon}^p_d = \left(\frac{2}{3} \dot{\boldsymbol{\varepsilon}}^p_d : \dot{\boldsymbol{\varepsilon}}^p_d \right)^{1/2} \tag{18}$$

($\dot{\varepsilon}^p_d$ worths the von Mises's norm of $\dot{\boldsymbol{\varepsilon}}^p_d$) and σ_{eq} is given by Eq.(4). In addition, we immediately obtain

$$\dot{\lambda} = \frac{1}{2C} \frac{\overline{\sigma}^2 \dot{\varepsilon}^p_d}{\sigma_{eq}};$$

reporting this result in Eq.(14), we get

$$\frac{\dot{\varepsilon}_m^p}{\dot{\varepsilon}_d^p} = \frac{1}{6C}\frac{\overline{\sigma}^2}{\sigma_{eq}}\left[\frac{2C\eta}{\overline{\sigma}^2}\left(\frac{3}{2}\boldsymbol{\sigma}' : \boldsymbol{X} + \eta\sigma_h\right) + 2q(g+1)(g+f)\frac{K}{\overline{\sigma}}sinh\left(K\frac{\sigma_h}{\overline{\sigma}}\right)\right]$$

or

$$\frac{\dot{\varepsilon}_m^p}{\dot{\varepsilon}_d^p} = \frac{\eta}{3\sigma_{eq}}\left(\frac{3}{2}\boldsymbol{\sigma}' : \boldsymbol{X} + \eta\sigma_h\right) + q(g+1)(g+f)\frac{K}{3C}\frac{\overline{\sigma}}{\sigma_{eq}}sinh\left(K\frac{\sigma_h}{\overline{\sigma}}\right). \tag{19}$$

The equations Eqs. (17, 19) (where $\dot{\boldsymbol{\varepsilon}}_d^p$ is defined by Eq.(16) and $\dot{\varepsilon}_d^p$ by Eq.(18)) consists of the plastic flow rule of the material.

3.2.3. Damage delocalization

In certain applications, especially those involving high stress and/or strain gradients, the porosity evolution equation undergoes a process of delocalization. In this context, we define local rates of porosity increase due to the voids growth. The local rates are determined by formula Eq.(6). The true non-local growth rate is then computed using the convolution formula presented below:

$$\begin{aligned} f(\mathbf{x}) &= \frac{1}{\mathrm{C}(\mathbf{x})}\int_\Omega \dot{f}_1(\mathbf{y})\chi(\mathbf{x}-\mathbf{y})\mathrm{d}\Omega_y \ , \\ C(\mathbf{x}) &= \textstyle\int_\Omega \chi(\mathbf{x}-\mathbf{y})\mathrm{d}\Omega_{\mathbf{y}} \ . \end{aligned} \tag{20}$$

Ω denotes here the studied domain and χ a weighting function, which we take the Gaussian of in practice:

$$\chi(\mathbf{z}) = exp\left(\frac{-|\mathbf{z}|^2}{l^2}\right), \tag{21}$$

where l serves as a characteristic length, approximately equal to the spacing between cavities, and it plays a role similar to the minimum mesh size in the Rousselier model. It is worth noting that this delocalization study has been extensively explored by Enakoutsa and colleagues ([24], [23] , and [26]) and in many other works including the pionnering work of Pijaudier-Cabot and Bazant [10] , but in the context of modelling of concrete materials.

4. Class of generalized standard materials and GLD model

Halphen and Nguyen [3]; Son [4] defined, within the framework of linearized theory, the class of "Generalized Standard Materials." (GSM) For these materials, the internal parameters collectively follow an extended normality law. Under these conditions, the local projection problem has a unique solution, provided that the evolution equations of the internal parameters are discretized in time with an implicit scheme. The GSM framework is largely explained in Appendix A of this paper.

Drawing inspiration from Enakoutsa [23], it can be shown that the model presented here defines a generalized standard material, provided that: (i) the framework considered is the linear theory; (ii) the porosity, orientation, and shape of the cavity are kept constant. Some elements of this proof are given in Appendix B

In practice, these restrictions are not realistic for problems involving ductile fracture which entail significant deformations, porosity growth, and cavity deformations. However, still following Enakoutsa [23], it can be observed that:

- if, in the hypoelasticity law, the additional terms due to the objective derivative of $\boldsymbol{\sigma}$ are discretized in time using an explicit scheme;
- if, in the criterion and flow rule, the porosity f and the shape factor S considered are those from the previous time step; then the equations of the local projection problem are exactly the same as in the linearized framework with fixed porosity f and shape factor S: thus, the model behaves as if the material were a generalized standard material.

Therefore, the existence and uniqueness of the solution to the local projection problem are ensured, provided that (i) the evolution equations of $\varepsilon^{\mathbf{P}}$ and $\bar{\epsilon}$ are discretized in time using an implicit scheme; (ii) the additional terms due to the objective derivative of $\boldsymbol{\sigma}$ are discretized in time using an explicit scheme; (iii) the values of porosity f and the quadratic form S used in the criterion and the flow rule are those from the previous time step.

5. Numerical implementation

5.1. Projection onto the yield surface

The essential problem of any numerical implementation of an elastic plastic model is that of the projection onto the yield surface. This problem is as follows: from the results of a " large elastic-plastic iteration" (elastic resolution over the whole structure with initial plastic deformations given), which provides the increment of total deformations $\nabla\dot{\varepsilon}$ between the time t and $t+\nabla t$ of the calculation, find the decomposition of $\dot{\varepsilon}$ into elastic $\dot{\varepsilon}^e$ and plastic $\dot{\varepsilon}^p$ (using the yield criterion at $t+\nabla t$ and the flow rule (between t and $t+\nabla t$)) and the stress at $t+\nabla t$.

In the subsequent, the quantities without indices are taken at the moment $t+\nabla t$ while those with an index "0" will be taken at the time t (it is therefore a question of known quantities.)

Let us begin, as in the case of the original Gurson's criterion, by defining a parametrization of the original Gurson's criterion of the criterion by means of an angle ϕ, ensuring automatic satisfaction. The flow rules will then provide an equation on ϕ which can be resolved numerically.

To find this parametrization, let us look for the maximum value of $C\frac{\sigma_{eq}^2}{\overline{\sigma}^2}$ corresponding to $\sigma_h = 0 \implies \cosh\left(K\frac{\sigma_h}{\overline{\sigma}}\right) = 1$; according to Eq. (1)

$$C\frac{\sigma_{eq}^2}{\overline{\sigma}^2} = (g+1)^2 + q^2(g+f)^2 - 2q(g+1)(g+f) = [g+1-q(g+f)]^2.$$

It is therefore natural to assume that

$$\begin{aligned} C\frac{\sigma_{eq}^2}{\overline{\sigma}^2} &= [g+1-q(g+f)]^2 cos^2\varphi \\ \Rightarrow \sigma_{eq} &= \frac{\overline{\sigma}}{\sqrt{C}}[g+1-q(g+f)]cos\varphi \end{aligned} \tag{22}$$

where φ is some angle with positive cosine. We get from Eq.(1)

$$
\begin{aligned}
2q(g+1)(g+f)cosh\left(K\frac{\sigma_h}{\overline{\sigma}}\right) &= (g+1)^2+q^2(g+f)^2-[g+1-q(g+f)]^2cos^2\varphi \\
&= (g+1)^2+q^2(g+f)^2-[g+1-q(g+f)]^2 \\
&\quad +[g+1-q(g+f)]^2sin^2\varphi \\
&= 2q(g+1)(g+f)+[g+1-q(g+f)]^2sin^2\varphi
\end{aligned}
$$

$$
\Rightarrow cosh\left(K\frac{\sigma_h}{\overline{\sigma}}\right) = 1+\frac{[g+1-q(g+f)]^2}{2q(g+1)(g+f)}sin^2\varphi
$$

$$
\Rightarrow \sigma_h = \frac{\overline{\sigma}}{K}sgn(\varphi)cosh^{-1}\left(1+\frac{[g+1-q(g+f)]^2}{2q(g+1)(g+f)}sin^2\varphi\right) \tag{23}
$$

where we introduce a "sgn(ϕ)" (sign of ϕ) to allow σ_h to take all possible values, both negative and positive. The Eqs. (22, 23) is the parametrization of the criterion we are looking for. The interval of variation of the angle ϕ can be taken equal to $\left[-\frac{\pi}{2},+\frac{\pi}{2}\right]$: it allows $cos(\phi)$ to take all positive or zero values, as well as $sgn(\phi)$ to take values ± 1. Before writing the flow rule in a discretized form, let us begin by establishing the relationships that exist between σ_h and σ_m on one hand, $\dot{\varepsilon}^p_d$ and $\dot{\varepsilon}^{p'}$ on the other hand. First, we get Eqs. (5)

$$
\begin{aligned}
\sigma_h =& \alpha_2\sigma_{\alpha\alpha}+(1-2\alpha_2)\sigma_{33} = \frac{1}{3}(\sigma_{\alpha\alpha}+\sigma_{33})+\left(\alpha_2-\frac{1}{3}\right)\sigma_{\alpha\alpha}+2\left(\frac{1}{3}-\alpha_2\right)\sigma_{33} \\
=& \sigma_m+(1-3\alpha_2)\left(-\frac{1}{3}\sigma_{\alpha\alpha}+\frac{2}{3}\sigma_{33}\right)
\end{aligned}
$$

which gives, from the definition Eq. (2) of the tensor $\boldsymbol{X}$:

$$
\sigma_h = \sigma_m+(1-3\alpha_2)\boldsymbol{\sigma}' : \boldsymbol{X}. \tag{24}
$$

In addition, from Eq. (16),

$$
\begin{aligned}
\dot{\boldsymbol{\varepsilon}}^p_d =& \dot{\boldsymbol{\varepsilon}}^p-3\alpha_2\dot{\varepsilon}^p_m\boldsymbol{e}_\alpha\otimes\boldsymbol{e}_\alpha-3(1-2\alpha_2)\dot{\varepsilon}^p_m\boldsymbol{e}_3\otimes\boldsymbol{e}_3 \\
=& \dot{\boldsymbol{\varepsilon}}^p-\dot{\varepsilon}^p_m\boldsymbol{e}_\alpha\otimes\boldsymbol{e}_\alpha-\dot{\varepsilon}^p_m\boldsymbol{e}_3\otimes\boldsymbol{e}_3+(1-2\alpha_2)\dot{\varepsilon}^p_m\boldsymbol{e}_\alpha\otimes\boldsymbol{e}_\alpha+2(3\alpha_2-1)\dot{\varepsilon}^p_m\boldsymbol{e}_3\otimes\boldsymbol{e}_3 \\
=& \dot{\boldsymbol{\varepsilon}}^p-3(1-3\alpha_2)\dot{\varepsilon}^p_m\boldsymbol{X}.
\end{aligned} \tag{25}
$$

Let us now write the flow rule in discretized form. $\Delta\boldsymbol{\varepsilon}^p_d$ being related to $\Delta\boldsymbol{\varepsilon}^{p'}$ par

the relationship

$$\Delta\boldsymbol{\varepsilon}_d^p = \Delta\boldsymbol{\varepsilon}^{p'} - 3(1-3\alpha_2)\Delta\varepsilon_m^p \boldsymbol{X} \tag{26}$$

(which is the discretized equivalent form of Eq.(25), we get (see Eq.(17) and Eq.(18))

$$\Delta\boldsymbol{\varepsilon}_d^p = \frac{3}{2}\frac{\Delta\boldsymbol{\varepsilon}_d^p}{\sigma_{eq}}\left(\boldsymbol{\sigma}' + \eta\sigma_h \boldsymbol{X}\right) \tag{27}$$

where

$$\Delta\boldsymbol{\varepsilon}_d^p = \left(\frac{3}{2}\Delta\boldsymbol{\varepsilon}_d^p : \Delta\boldsymbol{\varepsilon}_d^p\right)^{1/2}. \tag{28}$$

Note that these equations correspond to an implicit algorithm with respect to all parameters except the porosity f. The symbol $\tilde{f}$ represents an explicit approximation of porosity on the half-interval $t + \frac{\Delta t}{2}$ given by

$$\frac{\Delta\varepsilon_m^p}{\Delta\varepsilon_d^p} = \frac{\eta}{3\sigma_{eq}}\left(\frac{3}{2}\boldsymbol{\sigma}' : \boldsymbol{X} + \eta\sigma_h\right) + q(g+1)(g+\tilde{f})\frac{K}{3C}\frac{\overline{\sigma}}{\sigma_{eq}} sinh\left(K\frac{\sigma_h}{\overline{\sigma}}\right). \tag{29}$$

The explicit character of the algorithm with respect to f (parameter governing softening) ensures its convergence, taking $\tilde{f}$ at $t + \frac{\Delta t}{2}$, and not at t or $t + \Delta t$, allowing us to optimize the precision of the algorithm:

$$\tilde{f} = f_0 + \dot{f}_0\frac{\Delta t}{2}. \tag{30}$$

Assume $\boldsymbol{\sigma}'_o$ and $\sigma_m^\star$ the deviatoric and the mean parts of the stresses tensor (at $t + \Delta t$) $\boldsymbol{\sigma}^\star$ "elastically calculated," that is by assuming that the increment of deformation $\Delta\boldsymbol{\varepsilon}$ is purely elastic; we get

$$\boldsymbol{\sigma}^{*'} = \boldsymbol{\sigma}'_o + 2\mu\Delta\boldsymbol{\varepsilon}' \quad \text{and} \quad \sigma_m = \sigma_{mo} + (3\lambda + 2\mu)\,\Delta\varepsilon_m. \tag{31}$$

$\boldsymbol{\sigma}'_o$ and $\sigma_m^\star$ are the known quantities during the operation of the "projection on the yield surface." Now let us evaluate $\boldsymbol{\sigma}'$ using Eqs.(31), Eqs.(26), Eq.(27))

$$
\begin{aligned}
\boldsymbol{\sigma}' =& \boldsymbol{\sigma}'_o + 2\mu\Delta\boldsymbol{\varepsilon}^{e'} = \boldsymbol{\sigma}'_o + 2\mu\Delta\boldsymbol{\varepsilon}' - 2\mu\Delta\boldsymbol{\varepsilon}^{p'} = \boldsymbol{\sigma}^{*'} - 2\mu\Delta\boldsymbol{\varepsilon}^{p'} \\
=& \boldsymbol{\sigma}^{*'} - 2\mu\Delta\boldsymbol{\varepsilon}^{p}_{d} - 6\mu(1-3\alpha_2)\Delta\varepsilon^{p}_{m}\boldsymbol{X} \\
=& \boldsymbol{\sigma}^{*'} - 3\mu\frac{\Delta\varepsilon^{p}_{d}}{\sigma_{eq}}\left(\boldsymbol{\sigma}' + \eta\sigma_h\boldsymbol{X}\right) - 6\mu(1-3\alpha_2)\Delta\varepsilon^{p}_{m}\boldsymbol{X}.
\end{aligned}
\tag{32}
$$

Contracting this equation with the tensor $\frac{3}{2}\boldsymbol{X}$ using Eq.(29)

$$
k = q(g+1)(g+\tilde{f})\frac{K}{3C}\overline{\sigma}sinh\left(K\frac{\sigma_h}{\overline{\sigma}}\right); \tag{33}
$$

we get

$$
\begin{aligned}
\frac{3}{2}\boldsymbol{\sigma}' : \boldsymbol{X} =& \frac{3}{2}\boldsymbol{\sigma}^{*'} : \boldsymbol{X} - 3\mu\frac{\Delta\varepsilon^{p}_{d}}{\sigma_{eq}}\left(\frac{3}{2}\boldsymbol{\sigma}' : \boldsymbol{X} + \eta\sigma_h\right) \\
& -6\mu(1-3\alpha_2)\left[\frac{\eta}{3\sigma_{eq}}\left(\frac{3}{2}\boldsymbol{\sigma}' : \boldsymbol{X} + \eta\sigma_h\right) + \frac{k}{\sigma_{eq}}\right]\Delta\varepsilon^{p}_{d}
\end{aligned}
$$

thus, adding $\eta\sigma_h$ to the two sides of the equations, we get:

$$
\begin{aligned}
\frac{3}{2}\boldsymbol{\sigma}' : \boldsymbol{X} + \eta\sigma_h =& \frac{3}{2}\boldsymbol{\sigma}^{*'} : \boldsymbol{X} + \eta\sigma_h - 3\mu\frac{\Delta\varepsilon^{p}_{d}}{\sigma_{eq}}\left(\frac{3}{2}\boldsymbol{\sigma}' : \boldsymbol{X} + \eta\sigma_h\right) \\
& - 2\mu\frac{\eta}{\sigma_{eq}}(1-3\alpha_2)\left(\frac{3}{2}\boldsymbol{\sigma}' : \boldsymbol{X} + \eta\sigma_h\right)\Delta\varepsilon^{p}_{d} - 6\mu(1-3\alpha_2)\frac{k}{\sigma_{eq}}\Delta\varepsilon^{p}_{d}
\end{aligned}
$$

$$
\begin{aligned}
\Rightarrow & \left[1 + 3\mu\frac{\Delta\varepsilon^{p}_{d}}{\sigma_{eq}} + 2\mu\eta(1-3\alpha_2)\frac{\Delta\varepsilon^{p}_{d}}{\sigma_{eq}}\right]\left(\frac{3}{2}\boldsymbol{\sigma}' : \boldsymbol{X} + \eta\sigma_h\right) \\
& = \frac{3}{2}\boldsymbol{\sigma}^{*'} : \boldsymbol{X} + \eta\sigma_h - 6\mu k(1-3\alpha_2)\frac{\Delta\varepsilon^{p}_{d}}{\sigma_{eq}}
\end{aligned}
$$

$$
\Rightarrow \frac{3}{2}\boldsymbol{\sigma}' : \boldsymbol{X} + \eta\sigma_h = \frac{a\Delta\varepsilon^{p}_{d} + b}{c\Delta\varepsilon^{p}_{d} + d} \tag{34}
$$

where

$$a = -6\mu k(1-3\alpha_2) \quad ; \quad b = \left(\frac{3}{2}\boldsymbol{\sigma}^{*\prime} : \boldsymbol{X} + \eta\sigma_h\right)\sigma_{eq} \; ;$$
$$c = 3\mu + 2\mu\eta(1-3\alpha_2) \quad ; \quad d = \sigma_{eq}. \tag{35}$$

Let's go back now to Eq.(32) by adding $\eta\sigma_h\boldsymbol{X}$ to the two sides of the equations; we obtain

$$\boldsymbol{\sigma}' + \eta\sigma_h\boldsymbol{X} = \boldsymbol{\sigma}^{*\prime} + \eta\sigma_h\boldsymbol{X} - 3\mu\frac{\Delta\varepsilon_d^p}{\sigma_{eq}}\left(\boldsymbol{\sigma}' + \eta\sigma_h\boldsymbol{X}\right) - 6\mu(1-3\alpha_2)\Delta\varepsilon_m^p\boldsymbol{X}$$
$$\Rightarrow \left(1 + 3\mu\frac{\Delta\varepsilon_d^p}{\sigma_{eq}}\right)\left(\boldsymbol{\sigma}' + \eta\sigma_h\boldsymbol{X}\right) = \boldsymbol{\sigma}^{*\prime} + \eta\sigma_h\boldsymbol{X} - 6\mu(1-3\alpha_2)\Delta\varepsilon_m^p\boldsymbol{X}.$$

In addition, by Eq.(32) we have

$$\sigma_m = \sigma_{mo} + (3\lambda + 2\mu)\,\Delta\varepsilon_m^e = \sigma_m^* - (3\lambda + 2\mu)\,\Delta\varepsilon_m^p$$
$$\Rightarrow \Delta\varepsilon_m^p = \frac{\sigma_m^* - \sigma_m}{3\lambda + 2\mu}, \tag{36}$$

thus, by reporting in the previous equation, we get

$$\left(1 + 3\mu\frac{\Delta\varepsilon_d^p}{\sigma_{eq}}\right)\left(\boldsymbol{\sigma}' + \eta\sigma_h\boldsymbol{X}\right) =$$
$$\boldsymbol{\sigma}^{*\prime} + \eta\sigma_h\boldsymbol{X} - \frac{6\mu}{3\lambda + 2\mu}(1-3\alpha_2)(\sigma_m^* - \sigma_m)\boldsymbol{X}. \tag{37}$$

Taking the von Mises norm $\|\|$ of the two sides of the equation, we get

$$\sigma_{eq} + 3\mu\Delta\varepsilon_d^p = \left\| \boldsymbol{\sigma}^{*\prime} + \eta\sigma_h \boldsymbol{X} - \frac{6\mu}{3\lambda + 2\mu}(1 - 3\alpha_2)(\sigma_m^* - \sigma_m)\boldsymbol{X} \right\|$$

$$\Rightarrow \Delta\varepsilon_d^p = \frac{1}{3\mu}\left(\left\| \boldsymbol{\sigma}^{*\prime} + \eta\sigma_h \boldsymbol{X} - \frac{6\mu}{3\lambda + 2\mu}(1 - 3\alpha_2)(\sigma_m^* - \sigma_m)\boldsymbol{X} \right\| - \sigma_{eq} \right). \tag{38}$$

Finally, using the flow rule Eq.(29) together with Eqs.(33, 34, 36) we obtain

$$\Delta\varepsilon_m^p = \frac{\sigma_m^* - \sigma_m}{3\lambda + 2\mu} = \left(\frac{\eta}{3\sigma_{eq}} \frac{a\Delta\varepsilon_d^p + b}{c\Delta\varepsilon_d^p + d} + \frac{k}{\sigma_{eq}} \right) \Delta\varepsilon_d^p$$

$$\Rightarrow \frac{\sigma_m^* - \sigma_m}{3\lambda + 2\mu}\sigma_{eq} - \left(\frac{\eta}{3} \frac{a\Delta\varepsilon_d^p + b}{c\Delta\varepsilon_d^p + d} + k \right) \Delta\varepsilon_d^p = 0. \tag{39}$$

Let us observe that $\Delta\varepsilon_d^p$ can be expressed as a function of ϕ and $\frac{3}{2}\boldsymbol{\sigma}' : \boldsymbol{X}$ thanks to Eq.(38), considering Eqs.(22, 23, 24). Thus, we can choose ϕ and $\frac{3}{2}\boldsymbol{\sigma}' : \boldsymbol{X}$ as principal unknowns. These equations satisfy Eqs.(34, 39) where the coefficients a, b, c, d are given by Eq.(35) (k itself being given by Eq.(33)) .

These equations can be solved numerically by Newton's method: the quantity $\frac{3}{2}\boldsymbol{\sigma}' : \boldsymbol{X}$ can be evaluated by solving Eq.(34), ϕ being calculated at each Newton's iteration on $\frac{3}{2}\boldsymbol{\sigma}' : \boldsymbol{X}$ by solving Eq.(39) by Newton iteration on ϕ. Once ϕ and $\frac{3}{2}\boldsymbol{\sigma}' : \boldsymbol{X}$ are determined, we deduced σ_{eq}, σ_h, and σ_m by Eqs.(22, 23, 24), and $\Delta\varepsilon_m^p$ and $\Delta\varepsilon_d^p$ by Eqs.(36, 38), $\boldsymbol{\sigma}' + \eta\sigma_h\boldsymbol{X}$ (and hence $\boldsymbol{\sigma}'$) by Eq.(37), $\Delta\boldsymbol{\varepsilon}_m^p$ by Eq.(27) and $\Delta\varepsilon^{p\prime}$ by Eq.(26). Thus, the operation of projection onto the yield locus has been carried out.

5.2. Evolution equations for the internal parameters

The first internal parameter is the porosity f. Adopting an implicit algorithm with respect to this quantity leads to unsolvable convergence problems. We therefore adopt an explicit algorithm where f (as it appears for example in Eqs.(22, 23) does not represent the true value of the porosity at time $t + \Delta t$ but the approximation given by

$$f = f_o + \dot{f}_o \Delta t \tag{40}$$

(f is therefore fixed throughout the passage from the instant t to instant $t+\Delta t$).

Of course, after convergence of the large elastic plastic iterations from t to $t+\Delta t$, f is updated for the next step thanks to the following formula, discretized equivalent of Eq.(6)

$$\Delta t = 3\left(1-\tilde{f}\right)\Delta\varepsilon_m^p. \tag{41}$$

The (approximate) value $\tilde{f}$ of the porosity in the half-interval (see Eq.(**??**)) is used here in order to improve the accuracy of the algorithm.

The second internal parameter is the shape factor S, also unknown "a priori". To determine it, we adopt an iterative algorithm of a "fixed point" type. The law of evolution of this parameter is the discretized equivalent of Eq.(7)

$$\Delta S = \frac{3}{2}h\Delta\varepsilon_{33}^{p'} + 3\left(\frac{1-3\alpha_1}{f}+3\alpha_2-1\right)\Delta\varepsilon_m^p. \tag{42}$$

We recall that h is an independent parameter, besides f and S, of the triaxiality $\boldsymbol{T}$ defined by Eq.(8). It is therefore necessary to calculate, in addition to σ_m as we saw above, $\|\boldsymbol{\sigma}'\|$, quantity which, we recall, is not equal to $\sigma_{eq} = \left(\|\boldsymbol{\sigma}' + \eta\sigma_h\boldsymbol{X}\|\right)$. By definition of the von Mises norm $\|\|$ defined by

$$\sigma_{eq}^2 = \|\boldsymbol{\sigma}' + \eta\sigma_h\boldsymbol{X}\|^2 = \frac{3}{2}\left(\boldsymbol{\sigma}' + \eta\sigma_h\boldsymbol{X}\right) : \left(\boldsymbol{\sigma}' + \eta\sigma_h\boldsymbol{X}\right)$$

$$= \frac{3}{2}\boldsymbol{\sigma}' : \boldsymbol{\sigma}' + 3\eta\sigma_h\boldsymbol{\sigma}' : \boldsymbol{X} + \eta^2 + \sigma_h^2 = \|\boldsymbol{\sigma}'\|^2 + 2\eta\sigma_h\left(\frac{3}{2}\boldsymbol{\sigma}' : \boldsymbol{X} + \eta\sigma_h\right) - \eta^2\sigma_h^2$$

$$\Rightarrow \|\boldsymbol{\sigma}'\| = \left[\sigma_{eq}^2 - 2\eta\sigma_h\left(\frac{3}{2}\boldsymbol{\sigma}' : \boldsymbol{X} + \eta\sigma_h\right) + \eta^2\sigma_h^2\right]^{1/2}. \tag{43}$$

This equation allows to evaluate $\|\boldsymbol{\sigma}'\|$ and therefore the triaxiality $\|\boldsymbol{T}\|$, the quantities σ_{eq}, σ_h, $\frac{3}{2}\boldsymbol{\sigma}' : \boldsymbol{X} + \eta\sigma_h$ being known elsewhere.

The third internal parameter is the hardening parameter $\overline{\sigma}$, or what amounts to the same via Eq.(9), the mean equivalent deformation $\overline{\varepsilon}$. We use a fixed point

algorithm to calculate this parameter, as for the shape form factor. The law of evolution used, discretized equivalent of Eq.(10), is

$$\left(1-\tilde{f}\right)\overline{\sigma}\Delta\overline{\varepsilon}=\boldsymbol{\sigma}:\Delta\boldsymbol{\varepsilon}^{p}. \tag{44}$$

Its use requires the calculation of $\boldsymbol{\sigma}:\Delta\boldsymbol{\varepsilon}^{p}$ according to known quantities. We get, from Eqs.(24, 26) and Eq.(27),

$$\begin{aligned}
\boldsymbol{\sigma}:\Delta\boldsymbol{\varepsilon}^{p} &= (\boldsymbol{\sigma}'+\sigma_m\mathbf{1}):\left(\Delta\boldsymbol{\varepsilon}^{p'}+\Delta\varepsilon_m^p\mathbf{1}\right)=\boldsymbol{\sigma}':\Delta\boldsymbol{\varepsilon}^{p'}+3\sigma_m\Delta\varepsilon_m^p\\
&=\boldsymbol{\sigma}':(\Delta\boldsymbol{\varepsilon}_d^p+3(1-3\alpha_2)\Delta\varepsilon_m^p\boldsymbol{X})+3\left(\sigma_h-(1-3\alpha_2)\boldsymbol{\sigma}':\boldsymbol{X}\right)\Delta\varepsilon_m^p\\
&=\boldsymbol{\sigma}':\Delta\boldsymbol{\varepsilon}_d^p+3\sigma_h\Delta\varepsilon_m^p\\
&=\boldsymbol{\sigma}':\frac{3}{2}\frac{\Delta\varepsilon_d^p}{\sigma_{eq}}\left(\boldsymbol{\sigma}'+\eta\sigma_h\boldsymbol{X}\right)+3\sigma_h\Delta\varepsilon_m^p\\
&=(\boldsymbol{\sigma}'+\eta\sigma_h\boldsymbol{X}):\frac{3}{2}\frac{\Delta\varepsilon_d^p}{\sigma_{eq}}\left(\boldsymbol{\sigma}'+\eta\sigma_h\boldsymbol{X}\right)-\frac{3}{2}\frac{\Delta\varepsilon_d^p}{\sigma_{eq}}\eta\sigma_h\boldsymbol{X}:(\boldsymbol{\sigma}'+\eta\sigma_h\boldsymbol{X})+3\sigma_h\Delta\varepsilon_m^p\\
&=\sigma_{eq}\Delta\varepsilon_d^p+3\sigma_h\Delta\varepsilon_m^p-\eta\frac{\sigma_h}{\sigma_{eq}}\left(\frac{3}{2}\boldsymbol{\sigma}':\boldsymbol{X}+\eta\sigma_h\right)\Delta\varepsilon_d^p
\end{aligned}$$

thus, the evolution equation of Eq.(44) of $\overline{\varepsilon}$ can be written as

$$\Delta\overline{\varepsilon}=\frac{1}{\left(1-\tilde{f}\right)\overline{\sigma}}\left[\sigma_{eq}\Delta\varepsilon_d^p+3\sigma_h\Delta\varepsilon_m^p-\eta\frac{\sigma_h}{\sigma_{eq}}\left(\frac{3}{2}\boldsymbol{\sigma}':\boldsymbol{X}+\eta\sigma_h\right)\Delta\varepsilon_d^p\right] \tag{45}$$

where all the quantities on the right side of the equation are known quantities.

The fourth internal parameter is the vector $\boldsymbol{e}_3$ parallel to the void axis. Its law of evolution Eq.(11) is discretized in an explicit way following the expression:

$$\Delta\boldsymbol{e}_3=\Delta\boldsymbol{\Omega}\cdot\left(\boldsymbol{e}_3\right)_o \tag{46}$$

where $\Delta\boldsymbol{e}$ designates the rotation increment of the manner, equals for example to the anti-symmetric part of the gradient of the displacement increment. $\left(\boldsymbol{e}_3\right)_o$ designating the vector $\boldsymbol{e}_3$ at the explicitly known instant t; therefore we can perform the correction of this vector given by Eq.(46) prior to any other calculation, without having to perform iterations.

5.3. Numerical treatment of the delocalization

This procedure uses an array $\mathcal{A}(\mathrm{I},\mathrm{J})$. The first index varies from 1 to 6, the second from 1 to the total number of Gauss points concerned by the delocalization (it identifies the Gauss point). The meanings of the different quantities $\mathcal{A}(\mathrm{I},\mathrm{J})$ are as follows:

- $\mathcal{A}(1,\ \mathrm{J}), \mathcal{A}(2,\mathrm{J}), \mathcal{A}(3,\mathrm{J})$: Current coordinates of Gaussian point J;
- $\mathcal{A}(4,\ \mathrm{J})$: Local porosity increment (between times t and $t+\Delta t$) at the Gaussian point J;
- $\mathcal{A}(5,\mathrm{J})$: Real increment (after convolution) of porosity at the Gaussian point J;
- $\mathcal{A}(6,\mathrm{J})$: Gauss point weight (for integration).

The calculation procedure is as follows: at all the iterations and for all the Gauss points, a program is used to calculate the coordinates and the weight of the Gauss point, subsequently storing them in $\mathcal{A}(1-3,\mathrm{J})$ and $\mathcal{A}(6,\mathrm{J})$. It also calls a sub-program, which evaluates the local porosity increment; the latter is stored in $\mathcal{A}(4,\ \mathrm{J})$. Once the convergence on the nodal imbalances has been obtained, another program is called which, thanks to a double loop on the Gauss points, performs the convolution operation. The actual porosity increment at the point J, stored in $\mathcal{A}(5,\ \mathrm{J})$, is transmitted to a program, which performs the final operation of calculating and storing the porosity at time t and $t+\Delta t$.

6. Numerical simulations: mesh size effects

This section delves into an investigation concerning the variations in mesh size and their impact on numerical simulations of ductile fracture problems. These simulations utilize both the local and nonlocal versions of the GLD model. Emphasizing the significance of this investigation is crucial and should not be underestimated. The primary rationale behind incorporating the non-local concept into the GLP model is to eliminate undesirable mesh size effects that often accompany finite element computations using this model. To evaluate these mesh size effects, there's no need for a comparison with experimental data. Instead, our focus will be on examining a hypothetical axisymmetric specimen with a pre-existing notch, constructed from 508 Cl.3 steel (in accordance with American Standards) and subjected to tension loading. Figure 1 illustrates a detailed mesh for this specimen, with a minimum element size of 0.15 mm in the central region.

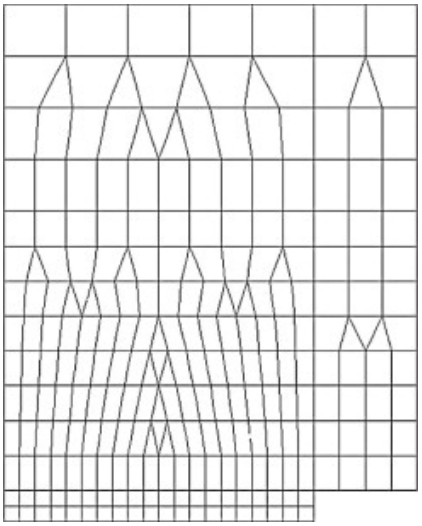

Figure 1: Fine mesh of the axisymmetric pre-notched specimen.

In Figure 2(a), we observe the predicted load-displacement curves for both of the considered mesh discretizations using the original Gurson model. The comparison between these curves reveals that altering the mesh discretization has no impact on crack initiation. However, a different scenario unfolds during the crack propagation phase: the curve's slope undergoes changes, and the disparity between the two curves progressively widens within the regions of material softening until the specimen ultimately ruptures. This discrepancy between the two curves highlights the problematic dependence of results predicted by the local GLD model on the size of the finite elements (FE). To clarify further, as the elements near the crack tip region decrease in size, failure occurs earlier, and crack propagation accelerates,

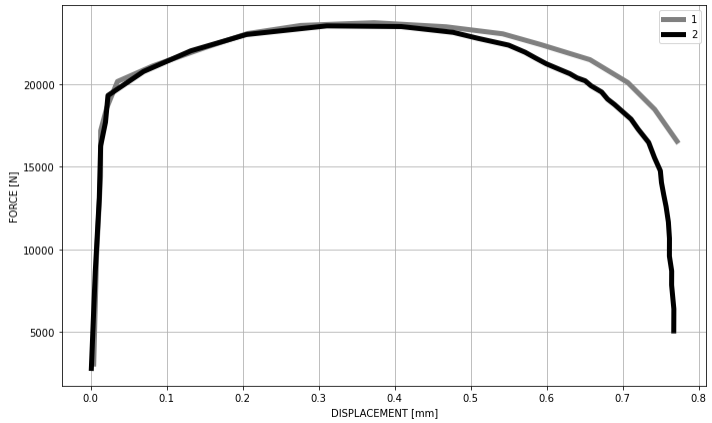

Figure 2: Predicted load versus displacement curves: calculations without damage delocalization; full black line (2): fine mesh, full grey line (1): crude mesh. The characteristic length scale used in the nonlocal calculations b is equal to 400 μm. Note the discrepancy between the two curves for the calculations without delocalization; this discrepancy is considerably reduced in the calculations with delocalization.

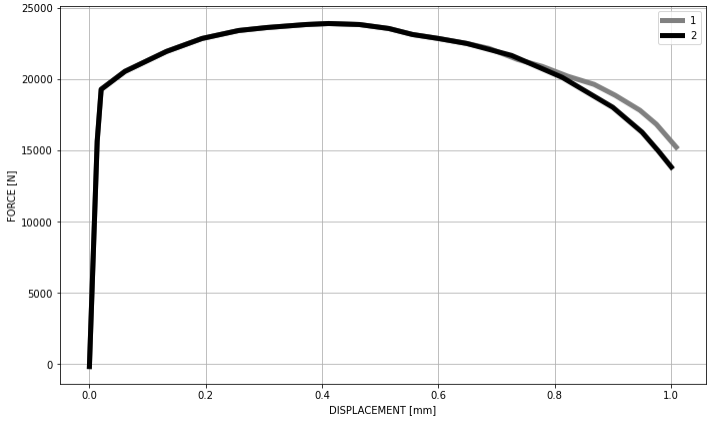

Figure 3: Predicted load versus displacement curves: calculations with damage delocalization; full black lines (2): fine mesh, full grey lines (1): crude mesh. The characteristic length scale used in the nonlocal calculations b is equal to 400 μm. Note the discrepancy between the two curves for the calculations without delocalization; this discrepancy is considerably reduced in the calculations with delocalization.

leading to a reduction in load-displacement curves. It's important to note that this mesh size sensitivity isn't related to the high stress and strain gradients near the crack tip. In fact, the mesh discretization in the crack propagation zone is sufficiently fine to capture significant spatial variations in the mechanical fields caused by crack propagation. The anomalous mesh size sensitivity observed in our simulations is a consequence of the presence of softening induced by damage growth.

This is a well-known issue that can lead to ill-posed mathematical problems when a characteristic length scale is absent in the model.

7. Numerical simulations of typical ductile fracture tests

For our initial application, we will conduct an axisymmetric simulation of Mudry's [7] fracture test on a round bar with axial symmetry. This bar, denoted as TA30 (with the number referring to its diameter), is composed of A508 Class 3 steel and features a pre-existing notch and crack. In Figure 4, you can see the geometry of the specimen and one of its discretizations.

To simplify the modeling, we are taking advantage of the symmetry along the horizontal mid-plane, which allows us to simulate only the upper half of the specimen. Furthermore, the axis of rotational symmetry aligns with the left boundary of the mesh. The specimen's dimensions are $90mm$ in height and $30mm$ in diameter. At the bottom of the mesh, there is a triangular-shaped central notch with an opening angle of 60 degrees and a depth of $5mm$.

Additionally, there is a fatigue-induced pre-crack measuring $1.7mm$ in length that originates from the root of the triangular notch. From this pre-crack's tip, a crack begins to propagate. This crack extends towards the axis of rotational symmetry and is situated slightly to the left of the notch root, where the element shapes transition from triangular to square.

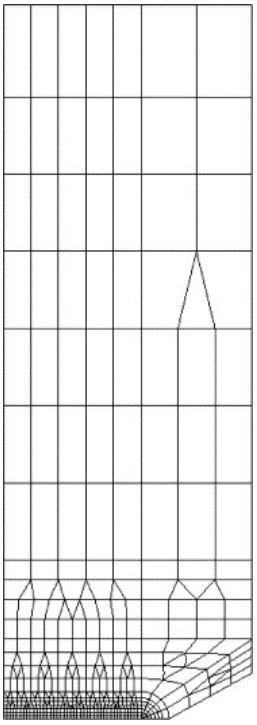

Figure 4: General mesh of the TA30 pre-cracked specimen - Minimum elements 200 microns.

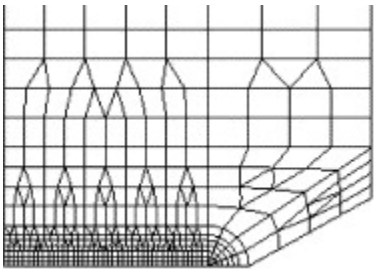

Figure 5: Zoom of the mesh of the TA30 specimen-Minimum element size 200 microns.

The characteristics of the material include, for the model with cavity shape effects, in addition to the usual parameters q, f_0, f_c, δ, σ_0, the cavity shape factor S_0, and the three components $(\mathbf{e}_3)_0^X$, $(\mathbf{e}_3)_0^Y$, $(\mathbf{e}_3)_0^Z$ of the unit vector $(\mathbf{e}_3)_0$ initially collinear with the void axis. These data are summarized in Table 1 as indicated of the Appendix C. These parameters are consistent with the ones utilized in Enakoutsa's [23] and Enakoutsa *et al.* [24] previous investigations of the same problem, except for the orientation and the shape factor. We will employ various values for the coalescence parameters, namely f_c (critical porosity) and δ (the "accelerating factor"), which differs from those considered by Enakoutsa's [23] and Enakoutsa *et al.* [24].

A decade ago, Enakoutsa's research [23] and the work conducted by Enakoutsa *et al.* [24] exposed a significant issue associated with excessive porosity smoothing in the Gurson's [5] model. To address this concern, it was recommended to employ the natural logarithm $(\log)$ instead of utilizing raw porosity values. In what follows. we shall repeat the same analysis for the GLD model of interest in this study.

7.1. Analysis of smoothing of porosity

The purpose of this section is to provide a theoretical explanation for the oversmoothing of porosity that occurs as a result of the nonlocal evolution equation Eq. (20). While this explanation may be basic and lacking in detail, it will be adequate to propose an effective solution.

When considering both the "mean" and deviatoric components of the flow rule Eq. $(12)_1$ and removing the plastic multiplier λ, we obtain the following equation Eq. (47):

$$\frac{\varepsilon_m^p}{\varepsilon_{eq}^p} = \frac{\eta}{3\sigma_{eq}}\left(\frac{3}{2}\boldsymbol{\sigma}' : \boldsymbol{X} + \eta\sigma_h\right) + q(g+1)(g+f)\frac{K}{3C}\frac{\overline{\sigma}}{\sigma_{eq}}sinh\left(K\frac{\sigma_h}{\overline{\sigma}}\right). \quad (47)$$

Here, ε^p_m is defined as $\frac{1}{3}$ tr ε^p, and ε^p_{eq} is defined as $\left(\frac{2}{3}\,\varepsilon^{p}_{ij}{}'\varepsilon^{p}_{ij}{}'\right)^{1/2}$, where $\varepsilon^{p,\prime}$ represents the deviatoric tensor of ε^p. These terms represent the mean and equivalent plastic strain rate, respectively.

If we utilize the local evolution equation Eq. (9) for porosity and combine it with the equation Eq. (47), we obtain (assuming simplicity during the pre-coalescence phase, where $f^* = f$ and $p = qf$):

$$\dot{f} = kf\varepsilon^p_{eq} \quad , \quad k \equiv \frac{\eta}{3\sigma_{eq}}\left(\frac{3}{2}\boldsymbol{\sigma}' : \boldsymbol{X} + \eta\sigma_h\right) + q(g+1)(g+f)\frac{K}{3C}\frac{\overline{\sigma}}{\sigma_{eq}} sinh\left(K\frac{\sigma_h}{\overline{\sigma}}\right). \tag{48}$$

If we replace the local equation (9) with the nonlocal one (20), this implies replacing equation $(48)_1$ with:

$$\dot{f}(\mathbf{x},t) = \frac{1}{A(\mathbf{x})}\,\left[\phi * (kf\varepsilon^p_{eq})\right](\mathbf{x},t) \tag{49}$$

Here, the symbol "$*$" represents the convolution product, and we have introduced indications of position and time dependence for clarity.

We begin by idealizing the body as an infinite medium and making the simplifying assumption that the parameters k and ε^p_{eq} in equation (49) exhibit spatial uniformity. This allows us to treat the factor $A(\mathbf{x})$ as uniform and incorporate it into the smoothing function ϕ. Moreover, the parameters k and ε^p_{eq} can be extracted from the convolution operation. Upon performing a spatial Fourier transformation of equation Eq. (49), we obtain the following expression:

$$\frac{\partial \hat{f}}{\partial t}(\mathbf{p},t) = k(t)\varepsilon^p_{eq}(t)\hat{\phi}(\mathbf{p})\hat{f}(\mathbf{p},t) \tag{50}$$

Alternatively, we can express this as:

$$\frac{\partial \hat{f}}{\partial \epsilon^p_{eq}}(\mathbf{p},\epsilon^p_{eq}) = k(\epsilon^p_{eq})\hat{\phi}(\mathbf{p})\hat{f}(\mathbf{p},\epsilon^p_{eq}) \tag{51}$$

Here, ϵ^p_{eq} represents the cumulative equivalent plastic strain, which is the time integral of ε^p_{eq}.

Equation (51) elucidates that the rate of growth of $\hat{f}(\mathbf{p}, \epsilon^p_{eq})$ is determined primarily by the factor $k(\epsilon^p_{eq})\hat{\phi}(\mathbf{p})$.

Now, if we consider the Fourier transform $\hat{\phi}(\mathbf{p})$ of a typical smoothing function, such as a Gaussian, it is noteworthy that this transform is positive and reaches its maximum at $\mathbf{p} = \mathbf{0}$. Consequently, the maximum growth rate of $\hat{f}(\mathbf{p}, \epsilon^p_{eq})$ occurs when $\mathbf{p} = \mathbf{0}$, corresponding to an infinite wavelength $\lambda \equiv 2\pi/|\mathbf{p}|$. This implies that Fourier components of f with longer wavelengths grow at a faster pace compared to those with shorter wavelengths, ultimately resulting in a gradual smoothing out of spatial variations in porosity.

To delve into more specifics, let's introduce the (albeit very simplistic) assumption that the quantity k is not only spatially uniform but also constant over time. When we integrate equation Eq. (51), we obtain the following expression:

$$\hat{f}(\mathbf{p}, \epsilon^p_{eq}) = \hat{f}(\mathbf{p}, 0)\, \exp\left[k\hat{\phi}(\mathbf{p})\epsilon^p_{eq}\right]. \tag{52}$$

Consequently, the evolution of $\hat{f}(\mathbf{p}, \epsilon^p_{eq})$ over time is controlled by the "growth factor" $\exp\left[k\hat{\phi}(\mathbf{p})\epsilon^p_{eq}\right]$.

Now, when we compare the growth factors for $\mathbf{p} = \mathbf{0}$ and $\mathbf{p} \neq \mathbf{0}$, we find:

$$\frac{\hat{f}(\mathbf{0}, \epsilon^p_{eq})/\hat{f}(\mathbf{0}, 0)}{\hat{f}(\mathbf{p}, \epsilon^p_{eq})/\hat{f}(\mathbf{p}, 0)} = \exp\left(k\left[\hat{\phi}(\mathbf{0}) - \hat{\phi}(\mathbf{p})\right]\epsilon^p_{eq}\right). \tag{53}$$

Since the function $\hat{\phi}(\mathbf{p})$ reaches its maximum at $\mathbf{p} = \mathbf{0}$, the term within the curly braces is positive. Consequently, this ratio is greater than one and can become significantly large for long times (large values of ϵ^p_{eq}) due to the rapid growth of the exponential function. This confirms that the development of Fourier components of f with longer wavelengths is significantly favored compared to those with shorter wavelengths.

It's worth noting that while the evolution equation (51) is not a diffusion equation, it exhibits characteristics reminiscent of such an equation. If we hypothetically consider a diffusion equation for porosity (with the cumulative equivalent plastic

strain ϵ_{eq}^p playing the role of time), expressed as:

$$\frac{\partial f}{\partial \epsilon_{eq}^p}(\mathbf{x}, \epsilon_{eq}^p) = D\,\Delta f(\mathbf{x}, \epsilon_{eq}^p), \tag{54}$$

where D is a constant and Δ denotes the Laplace operator, then taking the Fourier transform of this equation yields:

$$\frac{\partial \hat{f}}{\partial \epsilon_{eq}^p}(\mathbf{p}, \epsilon_{eq}^p) = -D\,|\mathbf{p}|^2 \hat{f}(\mathbf{p}, \epsilon_{eq}^p), \tag{55}$$

and upon integration, we obtain:

$$\hat{f}(\mathbf{p}, \epsilon_{eq}^p) = \hat{f}(\mathbf{p}, 0)\,\exp(-D\,|\mathbf{p}|^2 \epsilon_{eq}^p). \tag{56}$$

The ratio of the growth factors for $\mathbf{p} = \mathbf{0}$ and $\mathbf{p} \neq \mathbf{0}$ in this case is precisely given by:

$$\frac{\hat{f}(\mathbf{0}, \epsilon_{eq}^p)/\hat{f}(\mathbf{0}, 0)}{\hat{f}(\mathbf{p}, \epsilon_{eq}^p)/\hat{f}(\mathbf{p}, 0)} = \exp(D\,|\mathbf{p}|^2 \epsilon_{eq}^p). \tag{57}$$

This result aligns with what we would obtain by expanding the term within square brackets in equation Eq. (53) to the second order in $\mathbf{p}$.

7.2. Numerical simulations and comparison with experiments

The specific approach presented in Section 7.1 was implemented for the simulations presented in this study.

Figure 6 provides a visual representation that vividly showcases the comparison between the experimental load-displacement curve and the numerical outcomes obtained by adjusting the model parameters discussed earlier. The local GLD model yields results that are reasonably acceptable, although their reliance on the mesh, as demonstrated in the previous section, is noteworthy. These results were all obtained using a fixed mesh size of 200 μm and a characteristic length scale of b = 500 μm.

Upon examining Figure 6, disparities between the experimental and simulation results become apparent. Several explanations may account for these differences. One possibility could be the underlying model assumptions or the simplifications used in its development. Another factor to consider is the precision of the material

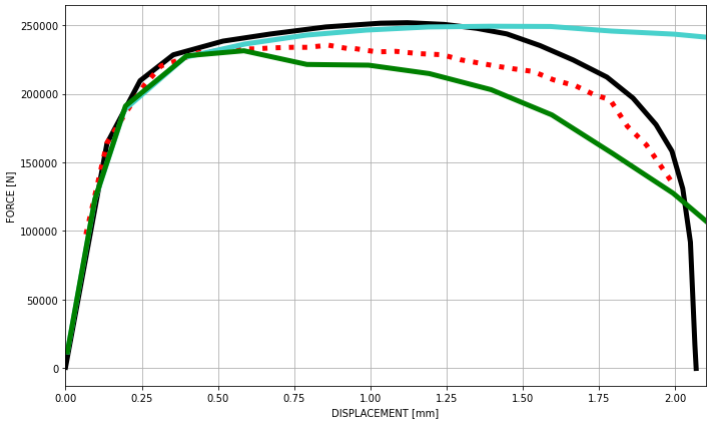

Figure 6: Comparison numerical predictions vs experimental results for the GLD model. Several values of the cavities growth acceleration factor δ were considered (Red: Experimental result; Green: GLD with $\delta = 2.8$; Black: GLD with $\delta = 2$; Blue: GLD with $\delta = 1.0$)

properties and parameters employed in the simulations, as they might not always be known with absolute certainty. Variations in material behavior or properties can introduce discrepancies in the results. This is why we varied the coalescence parameter, specifically the coalescence acceleration factor δ in the model. The substantial disparity observed in the descending portion of the experimental curve highlights the importance of accounting for coalescence to accurately replicate the test. This underscores that the previously reported agreement is contingent on various factors.

In light of the observed disparities between the experimental and simulation results as elucidated in Figure 6, it is imperative to delve deeper into the factors contributing to these differences. We have already considered the possibility of discrepancies arising from the underlying model assumptions and simplifications, as well as the precision of material properties and parameters utilized in our simulations. However, a comprehensive investigation into the effects of coalescence necessitates a more comprehensive analysis.

To accomplish this, we propose a multifaceted approach. First, we should extend our sensitivity analyses beyond the coalescence acceleration factor δ. We must systematically vary other critical parameters within the model, such as the initial conditions, boundary conditions, and possibly the numerical schemes employed. This broader exploration will enable us to pinpoint which aspects of the simulation are most sensitive to changes and contribute significantly to the observed disparities.

Furthermore, it is worth considering alternative material models or material property databases that may better capture the behavior of the materials under study. Such alternative models could provide a more accurate representation of the ex-

perimental data, thus reducing the discrepancies between the two. Additionally, we should investigate the potential influence of experimental uncertainties, such as measurement errors or environmental conditions, on our results.

In parallel, a rigorous validation process is essential to ensure the fidelity of our simulation approach. This validation should include comparing our simulations not only with the current experimental data but also with historical data and data from similar studies if available. By doing so, we can assess whether the observed disparities are unique to our current experimental setup or if they are indicative of a broader issue with the simulation methodology.

Finally, our approach to addressing the disparities between experimental and simulation results should encompass an in-depth exploration of model parameters, consideration of alternative material models, investigation of experimental uncertainties, and a thorough validation process. Through these concerted efforts, we aim to refine our simulation approach, enhance our understanding of the underlying physical processes, and ultimately achieve better agreement between our simulations and experimental data in future experiments.

8. Conclusion

In conclusion, this paper has presented a comprehensive and rigorous exploration of the Gologanu-Leblond-Devaux (GLD) model, showcasing its advanced capabilities in predicting ductile fractures in porous metals. The GLD model, building upon Gurson's foundation, offers a significant leap in fracture mechanics by accounting for cavity shape effects and nonlocal strain localization. The compatibility of the GLD model with generalized standard materials has been established, highlighting its potential for widespread application.

One crucial aspect emphasized in this study is the uniqueness of solutions in the numerical implementation, necessitating a meticulously devised mixed implicit/explicit algorithm. Through rigorous comparisons with experimental data and the introduction of a damage delocalization approach rooted in the natural logarithm of porosity, our research has provided compelling evidence of the GLD model's superior performance compared to the original porosity rate-based models. Furthermore, the profound theoretical elucidation of this phenomenon through Fourier's analysis of porosity rate adds depth to our understanding of ductile fracture behavior.

In summary, this work not only enhances our comprehension of ductile fracture phenomena but also establishes a robust numerical framework for predictive modeling. The GLD model emerges as a powerful and indispensable tool for the accurate analysis and prediction of fracture behavior in porous materials, pushing the boundaries of materials science and engineering.

References

[1] Mandel, J., 1964. Contribution théorique à l'étude de l'écrouissage et des lois d'écoulement plastique, *Proceedings of the 11th International Congress on Applied Mechanics*, Springer, pp. 502-509 (in French)

[2] Hill, R., 1967. The essential structure of constitutive laws for metal composites and polycrystals, *Journal of Mechanics and Physics of Solids*, **15**, 79-95

[3] Halphen B. and Nguyen Q.S., 1975. Sur les matériaux standards généralisés, *Journal de Mécanique*, Journal de Mécanique, **14**: 39-63.

[4] Son, N.Q., 1977. On the elastic plastic initial-boundary value problem and its numerical integration. International Journal for Numerical Methods in Engineering **11**, 817–832.

[5] Gurson A.L. (1977). Continuum theory of ductile rupture by void nucleation and growth: Part I - yield criteria and flow rules for porous ductile media, *ASME J. Engng. Mater. Technol.*, **99**, 2-15

[6] Tvergaard V., 1981. "Influence of voids on shear band instabilities under plane strain conditions," *Int. J. Fracture*, **17**, 389-407.

[7] G. Rousselier, F. Mudry, 1980. Etude de la rupture ductile de l'acier faiblement allié en Mn-Ni-Mo pour cuves de réacteurs à eau ordinaire sous pression, approvisionné sous la forme d'une débouchure de tubulure. Résultats du programme expérimental, EdF Centre des Renardières Internal Report HT/PVD529 MAT/T43 (in French).

[8] Tvergaard V. and Needleman A., 1984. Analysis of cup-cone fracture in a round tensile bar, *Acta Metall.*, **32**, 157-169

[9] Pijaudier-Cabot, G. and Bazant, Z.P., 1987. Nonlocal Damage Theory, *ASCE J. Engrg. Mech.*, **113**, 1512-1533

[10] Pijaudier-Cabot, G., and Bazant, Z. P., 1987. Nonlocal damage theory. *Journal of Engineering Mechanics*, **113**(10), 1512-1533.

[11] Perrin, G, and Leblond, J-B, 1990. Analytical study of a hollow sphere made of plastic porous material and subjected to hydrostatic tension: Application to some problems in ductile fracture of metals, *Int J Plast.* ; **6**: 677–699.

[12] Lee, B.J., and Mear, M.E., 1992. Axisymmetric deformation of power-law solids containing a dilute concentration of aligned spheroidal voids, *J. Mech. Phys. Solids*, **40**, 1805-1836.

[13] Perrin, G., 1992. Contribution à l' étude théorique et numérique de la rupture ductile des métaux. Thèse de Doctorat, Ecole Polytechnique, Palaiseau, France

[14] Gologanu, M., Leblond, J.B., and Devaux, J., 1993. Approximate models for ductile metals containing non-spherical voids - Case of axisymmetric prolate ellipsoidal cavities, *J. Mech. Phys. Solids*, **41**, 1723-1754.

[15] Howard, I.C., Li, Z.H., Bilby, B.A., 1994. "Ductile crack growth predictions for large center cracked panels by damage modeling using 3-D finite element analysis," *Fatigue and Fracture Engrg. Mater. Struct.* **17**, 959-969

[16] Leblond, J.B., Perrin, G., and Devaux, J., 1994. Bifurcation Effects in Ductile Metals with Nonlocal Damage, *ASME J. Applied . Mech.*, **6**1, 236-242.

[17] Gologanu, M., Leblond, J.B., and Devaux, J., 1994. Approximate models for Recent Extensions of Gurson's Model for ductile metals containing non-spherical voids - Case of axisymmetric oblate ellipsoidal cavities, *ASME J. Eng. Mat. Tech.*, 116, 290-297.

[18] Tvergaard V. and Needleman A., 1995. "Effects of Nonlocal Damage in Porous Plastic Solids", *Int. J. Solids Struct.,* **32**, 1063-1077

[19] Gologanu M., Leblond J.B., Perrin G. and Devaux J., 1997. "Recent extensions of Gurson's model for porous ductile metals," in: *Continuum Micromechanics*, CISM Courses and Lectures 377, P. Suquet ed., Springer, pp. 61-130

[20] Tvergaard, V. and Needleman, A., 1997. "Nonlocal Effects on Localization in a Void-sheet", *International Journal of Solids and Structures,* **34**, 2221-2238

[21] Z. Li and M. Huang, 2005. Combined effects of void shape and void size - oblate spheroidal microvoid embedded in infinite non-linear solid. *Int. J. Plasticity,* **21**(3):625–650.

[22] J. Wen, Y. Huang, K.C. Hwang, C. Liu, and M. Li, 2005. The modified Gurson model accounting for the void size effect. *Int. J. Plasticity*, **21**(2):381–395.

[23] Enakoutsa, K., 2007. Modèle Non-locaux en Rupture Ductile des Métaux. Ph.D thesis, Université Pierre et Marie Curie (Paris VI) (in French)

[24] Enakoutsa K., Leblond J.B. and Perrin G., 2007. "Numerical Implementation and Assessment of a Phenomenological Nonlocal Model of Ductile Rupture," *Computational Methods in Applied Mechanics and Engineering*, **196**, 1946-1957

[25] V. Monchiet, O. Cazacu, E. Charkaluk, and D. Kondo, 2008. Approximate criteria for anisotropic metals containing non spherical voids. *Int. J. Plasticity,* **24**:1158– 1189.

[26] Enakoutsa K., and Leblond J.B., 2009. "Numerical Implementation and Assessment of the GLPD Micromorphic Model of Ductile Rupture," *European Journal of Mechanics A/Solids*, **28**, 445-460

[27] Enakoutsa, K., 2012. "Some new Applications of the GLPD Micromorphic Model of Ductile Fracture," *Mathematics and Mechanics of Solids,* **19**(3), 242-259

[28] Z. Li and P. Steinmann, 2006. Rve-based studies on the coupled effects of void size and void shape on yield behavior and void growth at micron scales. *Int. J. Plasticity*, **22**(7):1195–1216.

[29] Enakoutsa, K., 2015 "Analytical applications and effective properties of a second gradient isotropic elastic material model," Zeitschrift fr angewandte Mathematik und Physik, **66**(3), 1277-1293

Appendix A. Class of Generalized Standard Materials and the GLD model

In this section, we aim to introduce Generalized Standard Materials (abbreviated as GSM) and then examine the generalized standard nature of the GLP model under the assumption of small deformations. It should be noted that the formalism of generalized standard materials only applies under this assumption.

The examination demonstrates that, at a fixed porosity, the constitutive equations of the GLD model possess the required properties to ensure the model's classification within the GSM class.

In the following section, we will explore the implications of this property concerning the numerical implementation of the model.

It is important to immediately note that this property applies equally to both the original local version of the model and its non-local modified version presented in Section 7.1, as fixing the porosity disregards its evolution equation, which is the only differing point between the two versions.

The presentation begins with a very brief general overview of some aspects of the work by Halphen and Nguyen [3] , and Nguyen [4] on the Generalized Strain Gradient (GSM). It continues by providing a simple example of MSG before delving into the main result of this section: the generalized standard nature of GLP model when the porosity, the orientation, and the shape factor components in the model are assumed to be discretized with an explicit numerical scheme.

Appendix A.1. Generalities

The constitutive law of an GSM is specified using two thermodynamic potentials. The first one is the specific free energy $\psi(\varepsilon, \boldsymbol{\alpha})$, which is a function of the strain tensor $\mathbf{v}$ and a set of internal parameters collectively denoted as $\boldsymbol{\alpha}$. This function must be convex with respect to the variables ε and α taken separately (but not necessarily with respect to the global variable (ε, α)).

The free energy provides by differentiation the stress tensor $\boldsymbol{\sigma}$ and the thermodynamic force $\mathbf{F}$ associated with α:

$$\boldsymbol{\sigma} = \frac{\partial \psi}{\partial \varepsilon} \quad \text{and} \quad \mathbf{F} = -\frac{\partial \psi}{\partial \alpha} \tag{A.1}$$

The second thermodynamic potential is the dissipation potential, denoted as $\mathcal{D}(\dot{\alpha})$, which must be a convex, positive, and zero function for $\dot{\alpha} = 0$. This potential governs the evolution equations of the internal parameters through the following equivalent relationships:

$$\mathbf{F} \in \partial \mathcal{D}(\dot{\alpha}) \iff \dot{\alpha} \in \partial \tilde{\mathcal{D}}(\mathbf{F}) \tag{A.2}$$

The notation $\tilde{\mathcal{D}}$ represents the Legendre-Fenchel transform. [3]

Here, $\partial\mathcal{D}$ and $\partial\tilde{\mathcal{D}}$ represent the sub-differentials of $\mathcal{D}$ and $\tilde{\mathcal{D}}$ respectively.

For a time-independent behavior, as is the case in our work, the potential $\mathcal{D}$ is positively homogeneous of degree 1 with respect to $\dot{\mathbf{a}}$.

Its Legendre-Fenchel transform, $\tilde{\mathcal{D}}(\mathbf{F})$, is then the indicator function[4] of a closed convex set $\mathcal{C}$ (the domain of reversibility) in the space of thermodynamic forces $\mathbf{F}$.

This set is defined by an inequality of the form $\Phi(\mathbf{F}) \leq 0$ for a certain function Φ, the sub-differential $\partial\tilde{\mathcal{D}}(\mathbf{F})$ is reduced to the zero vector $\mathbf{0}$ if $\mathbf{F}$ is contained within the convex set $\mathcal{C}$, coincides with the half-line $\eta(\partial f/\partial\mathbf{F})(\mathbf{F}), \eta \geq 0$ if $\mathbf{F}$ is on the boundary of $\mathcal{C}$, and is empty if $\mathbf{F}$ is not contained in $\mathcal{C}$.

The evolution equation $[\text{A.2}]_2$ can thus be rewritten in an equivalent form:

$$\dot{\mathbf{a}} = \eta\frac{\partial\Phi}{\partial\mathbf{F}} \quad , \quad \eta = \begin{cases} 0 & \text{if} \quad \Phi(\mathbf{F}) < 0 \\ \geq 0 & \text{if} \quad \Phi(\mathbf{F}) = 0 \end{cases} \tag{A.3}$$

This means that the evolution equation of $\mathbf{a}$ follows a kind of generalized "normality property."

This immediately leads to a number of properties that the GSMs satisfy:

Appendix A.2. Properties of the GSMs

Appendix A.2.1. Property 1

The evolution law [A.3] of $\mathbf{a}$ *ensures the positiveness of the dissipation* $\mathbf{F} : \dot{\mathbf{a}}$.

Indeed, the sub-differential of $\mathcal{D}(\dot{\mathbf{a}})$ is defined as:

$$\mathbf{F} \in \partial\mathcal{D}(\dot{\mathbf{a}}) \iff \forall\dot{\mathbf{a}}', \quad \mathbf{F} : (\dot{\mathbf{a}}' - \dot{\mathbf{a}}) \leq \mathcal{D}(\dot{\mathbf{a}}') - \mathcal{D}(\dot{\mathbf{a}}). \tag{A.4}$$

For $\dot{\mathbf{a}}' = 0$, this gives $-\mathbf{F} : \dot{\mathbf{a}}' \leq -\mathcal{D}(\dot{\mathbf{a}})$ (since $\mathcal{D}(\mathbf{0}) = 0$), which means $\mathbf{F} : \dot{\mathbf{a}}' \geq \mathcal{D}(\dot{\mathbf{a}}) \geq 0$ (due to the positiveness of $\mathcal{D}$).

Appendix A.2.2. Property 2

Let's agree that quantities indexed by ^{0} *are taken at time* t*, and those without a particular symbol are taken at time* $t + \Delta t$*. If the evolution equation [A.3] for* α *is discretized in time using an implicit scheme, then the projection problem, which consists of determining the values of* α *or* $\Delta\alpha \equiv \alpha - \alpha^0$ *based on the values of* ε^0*,* $\alpha^{\mathbf{0}}$*, and* $\Delta \equiv \varepsilon - \varepsilon^0$*, is equivalent to minimizing the function* $\chi(\varepsilon, \alpha^{\mathbf{0}}, \mathbf{\Delta}\alpha) \equiv \psi(\varepsilon, \alpha^{\mathbf{0}} + \mathbf{\Delta}\alpha) + \mathcal{D}(\mathbf{\Delta}\alpha)$ *with respect to* $\Delta\alpha$.

[3] It is recalled that: (i) the Legendre-Fenchel transform $\tilde{f}(\mathbf{y})$ of the function $f(\mathbf{x})$ is defined by the formula $\tilde{f}(\mathbf{y}) \equiv \sup_{\mathbf{x}}[\mathbf{x}\cdot\mathbf{y} - f(\mathbf{x})]$; (ii) its subdifferential $\partial f(\mathbf{x})$ at point $\mathbf{x}$ is the set of points $\mathbf{y}$ such that $\mathbf{y}\cdot(\mathbf{x}' - \mathbf{x}) \leq f(\mathbf{x}') - f(\mathbf{x})$ for all points $\mathbf{x}'$; (iii) the equivalence $\mathbf{y} \in \partial f(\mathbf{x}) \iff \mathbf{x} \in \partial\tilde{f}(\mathbf{y})$ follows.

[4] Recall that the indicator function of a convex set takes the values 0 and $+\infty$ inside and outside the set, respectively.

To establish this property, let's note that the condition ensuring that the function χ is minimal at the point $\Delta\alpha$ is given by:

$$\mathbf{0} \in \partial\chi(\varepsilon, \alpha^{\mathbf{0}}, \mathbf{\Delta}\alpha) \iff \mathbf{0} \in \frac{\partial\psi}{\partial\alpha}(\varepsilon, \alpha^{\mathbf{0}} + \mathbf{\Delta}\alpha) + \partial\mathcal{D}(\alpha) \iff$$
$$-\frac{\partial\psi}{\partial\alpha}(\varepsilon, \alpha^{\mathbf{0}}, \mathbf{\Delta}\alpha) \in \partial\mathcal{D}(\alpha) \iff \mathbf{F} \in \partial\mathcal{D}(\Delta\alpha)$$

where $\mathbf{F}$ represents the thermodynamic force at time $t + \Delta t$.

The announced equivalence is then clear since the last expression is nothing but the evolution equation of α, written in the form $[A.2]_1$ instead of $[A.2]_2$, and discretized implicitly in time.

(Note that $\partial\mathcal{D}\left(\frac{\Delta\alpha}{\Delta t}\right) = \partial\mathcal{D}(\Delta\alpha)$ since $\mathcal{D}$ is positively homogeneous of degree 1).

Since the functions $\psi(\varepsilon, \alpha^{\mathbf{0}} + \mathbf{\Delta}\alpha)$ and $\mathcal{D}\Delta\alpha$ are convex with respect to $\Delta\alpha$, this equivalence guarantees the existence of the solution to the projection problem, and its uniqueness if the free energy is *strictly* convex[5] with respect to α.

It also ensures the symmetry of the tangent matrix to be used to solve the projection problem, since this matrix is the Hessian matrix of the function χ.

Appendix A.2.3. Property 3

The tangent matrix of global elasto-plastic iterations is symmetric.

This third property is somewhat less obvious than the first two and arises from the second property. To establish it, we will employ a vector notation for stress and strain tensors: $\varepsilon \equiv (\varepsilon_i) 1 \leq i \leq 6$, $\boldsymbol{\sigma} \equiv (\sigma_i) 1 \leq i \leq 6$, along with internal variables: $\alpha \equiv (\alpha_p) 1 \leq p \leq N$. The relevant tangent matrix is then $(\partial\sigma_i/\partial\varepsilon_j) 1 \leq i, j \leq 6$ where $\boldsymbol{\sigma}$ is expressed as a function of the unique variable ε using the expression:

$$\boldsymbol{\sigma} \equiv \frac{\partial\psi}{\partial\varepsilon}[\varepsilon, \alpha(\varepsilon)] \tag{A.5}$$

Here, $\alpha(\varepsilon) = \alpha^{\mathbf{0}} + \mathbf{\Delta}\alpha(\varepsilon)$, and $\Delta\alpha(\varepsilon)$ minimizes the function $\chi(\varepsilon, \alpha^0, \Delta\alpha)$.

By differentiating equation [A.5], we obtain:

$$\frac{\partial\sigma_i}{\partial\varepsilon_j}(\varepsilon) = \frac{\partial^2\psi}{\partial\varepsilon_i\partial\varepsilon_j}(\varepsilon, \alpha(\varepsilon)) + \frac{\partial^2\psi}{\partial\varepsilon_i\partial\alpha_p}(\varepsilon, \alpha(\varepsilon))\frac{\partial\Delta\alpha_p}{\partial\varepsilon_j}(\varepsilon) \tag{A.6}$$

To evaluate the derivatives $\partial\Delta\alpha_p \Big/ \partial\varepsilon_j$, we differentiate the conditions $\partial\chi/\partial\Delta\alpha_p = 0$ defining $\Delta\alpha$ with respect to ε_j, using the definition of the function χ:

[5] The dissipation potential cannot be strictly convex, as its property of positive degree 1 homogeneity implies linearity along each half-line starting from the origin $\mathbf{0}$.

$$\frac{\partial^2\psi}{\partial\varepsilon_j\partial\alpha_p}(\varepsilon,\alpha(\varepsilon))+\frac{\partial^2\mathcal{D}}{\partial\Delta\alpha_p\partial\Delta\alpha_q}(\Delta\alpha(\varepsilon))\frac{\partial\Delta\alpha_q}{\partial\varepsilon_j}(\varepsilon)=0. \tag{A.7}$$

Let $\mathbf{M}$ denote the inverse of the Hessian matrix $(\partial^2\mathcal{D}\Big/\partial\Delta\alpha_p\partial\Delta\alpha_q)_{1\leq p,q\leq N}$.

Inverting equation [A.7], we obtain:

$$\frac{\partial\Delta\alpha_p}{\partial\varepsilon_j}(\varepsilon)=-M_{pq}(\Delta\alpha(\varepsilon))\frac{\partial^2\psi}{\partial\varepsilon_j\partial\Delta\alpha_q}(\varepsilon,\alpha(\varepsilon)) \tag{A.8}$$

Substituting this result into equation [A.6], we have:

$$\frac{\partial\sigma_i}{\partial\varepsilon_j}(\varepsilon)=\frac{\partial^2\psi}{\partial\varepsilon_i\partial\varepsilon_j}(\varepsilon,\alpha(\varepsilon))-\frac{\partial^2\psi}{\partial\varepsilon_i\partial\alpha_p}(\varepsilon,\alpha(\varepsilon))M_{pq}(\Delta\alpha(\varepsilon))\frac{\partial^2\psi}{\partial\varepsilon_j\partial\Delta\alpha_q}(\varepsilon,\alpha(\varepsilon)), \tag{A.9}$$

which clearly reveals the symmetry of the matrix $(\partial\sigma_i\Big/\partial\varepsilon_j)_{1\leq i,j\leq 6}$.

In summary, from the above, three main insights can be drawn.

The first insight pertains to the convexity of the function $\varphi(+\Delta\varepsilon,\alpha+\mathbf{\Delta}\alpha)+\mathcal{D}(\mathbf{\Delta}\alpha)$ with respect to the variable $\Delta\alpha$. This ensures the existence of the minimum, and consequently, the solution to the "projection problem."

The second insight concerns the uniqueness of the solution to the projection problem. It is achieved under the condition that φ is strictly convex with respect to the variable α. It should be noted that $\mathcal{D}$ is convex but not strictly so, as it is positively homogeneous of degree 1.

The third insight, finally, pertains to the symmetry of the tangent matrix necessary for minimizing $\chi(\varepsilon,\alpha^0,\Delta\alpha)\equiv\psi(\varepsilon,\alpha^0,\Delta\alpha)+\mathcal{D}(\Delta\alpha)$ with respect to $\Delta\alpha$. Therefore, there is symmetry in the tangent matrix within the projection problem.

Appendix B. The GLD model and the MSG framework

To begin with, it is necessary to define the state variables and the expression for the free energy, and then ensure that the latter satisfies the required properties (see Appendix A above).

The state of the material is described by the following state variables: the components of total deformation ε and a set of internal variables including the components of plastic deformation ε^p and the cumulative equivalent plastic deformation.

We then propose the following free energy potential, which is the sum of elastic deformation energy and "locked" hardening energy:

$$\psi(\varepsilon, \varepsilon^p, \varepsilon_{eq}) = \frac{1}{2}(\varepsilon - \varepsilon^p) : \mathbf{C} : (\varepsilon - \varepsilon^p) + \lambda \int_0^{\varepsilon_{eq}} \sigma(\varepsilon) \mathrm{d}\varepsilon. \tag{B.1}$$

In this equation, $\mathbf{C}$ represents the fourth-order elastic stiffness tensor, and $\sigma(\varepsilon_{eq})$ is the yield stress in simple tension, a function of cumulative plastic deformation.

It is easy to see, with this definition, that the free energy ψ is *strictly convex* with respect to the internal variable ε, as the quadratic form defined by $\mathbf{C}$ is positive definite. The free energy is also strictly convex with respect to ε^p for the same reason as mentioned earlier. It is also strictly convex with respect to the variable ε_{eq} due to the positivity of the hardening slope. Furthermore, it is a sum of strictly convex functions of ε^p and ε_{eq} (with ε fixed). Therefore, the free energy is strictly convex with respect to the global internal variable $(\varepsilon^p, \varepsilon_{eq})$, as desired.

Moreover, the derivative of ψ with respect to ε is equal to $\boldsymbol{\sigma}$, as desired as well, and the thermodynamic forces $\mathbf{F}^{\varepsilon^p}$ and $F^{\varepsilon_{eq}}$ associated with the internal variables ε^p and ε_{eq} are given by:

$$\begin{cases} \mathbf{F}^{\boldsymbol{\varepsilon}^p} = -\dfrac{\partial \psi}{\partial \boldsymbol{\varepsilon}^p} = \mathbf{C} : (\boldsymbol{\varepsilon} - \boldsymbol{\varepsilon}^p) = \mathbf{s} \\ F^{\varepsilon_{eq}} = -\dfrac{\partial \psi}{\partial \varepsilon_{eq}} = -\sigma(\varepsilon_{eq}) \equiv \sigma \end{cases} \tag{B.2}$$

The second thing to do is to demonstrate that the reversibility domain defined by GLD criterion in the space of thermodynamic forces (expressing GLD's charge function Φ in terms of the variables $\mathbf{F}^{\varepsilon^p}$ and $F^{\bar{\epsilon}}$ instead of $\boldsymbol{\sigma}$ and $\bar{\sigma}$) is convex.

The transformation from the variables ($\boldsymbol{\sigma}$, $\bar{\sigma}$) to the variables ($\mathbf{F}^{\varepsilon^p}$, $F^{\bar{\epsilon}}$) = $(\boldsymbol{\sigma}, -\lambda\bar{\sigma})$ is, however, linear. Therefore, it will be sufficient to prove that the reversibility domain in the space of the first variables, $\mathcal{C} \equiv (\boldsymbol{\sigma}, \bar{\sigma})$; $\quad \Phi(\boldsymbol{\sigma}, \bar{\sigma}, S, f) \leq 0$, is convex.

This would result immediately from the convexity of GLD's charge function Φ with respect to the global internal variable ($\boldsymbol{\sigma}$, $\bar{\sigma}$), if this function were convex.

The second element consists of checking that the evolution equations of the internal variables $\varepsilon^{\mathbf{P}}$ and $\bar{\epsilon}$ comply with the generalized normality property with respect to the GLD's yield function, expressed in terms of thermodynamic forces:

$$\left\{\begin{array}{lcl} \dot{\varepsilon}^{p} & = & \eta\dfrac{\partial\Phi}{\partial\mathbf{F}^{\varepsilon^{\mathbf{P}}}} \equiv \eta\dfrac{\partial\Phi}{\partial\boldsymbol{\sigma}} \\ \dot{\bar{\epsilon}} & = & \eta\dfrac{\partial\Phi}{\partial F^{\bar{\epsilon}}} \equiv -\dfrac{\eta}{\lambda}\dfrac{\partial\Phi}{\partial\bar{\sigma}} \end{array}\right. \tag{B.3}$$

The two last elements of this proof were extensively discussed in Enakoutsa *et al.* [24] and Enakoutsa [23] in the context of the Gurson's [5] model, and for this reason will not be repeated here.

Appendix C. Parameters of the GLD model

The material parameters utilized for the simulations presented above are precisely delineated as follows:

Parameter	Values
E (MPa)	203 000
ν	0.3
σ_0 (MPa)	450
q	1.47
f_0	0.00016
f_c	0.05
$b(\mu$m)	500
δ	2.8
S_0	2.1
$(\mathbf{e}_3)_0^X$	0.
$(\mathbf{e}_3)_0^Y$	0.
$(\mathbf{e}_3)_0^Z$	1.

Table C.1: Material parameters used for the numerical simulations on the pre-cracked TA and the axisymmetric pre-notched specimens. The characteristics of the material include, for the model with shape effects, in addition to the usual ones such as q, f_0, f_c, δ, b, the initial shape factor S_0 and the three components $(\mathbf{e}3)_0^X$, $(\mathbf{e}3)_0^Y$, $(\mathbf{e}3)_0^Z$ of the unit vector $(\mathbf{e}3)0$ initially collinear with the void axis.